nature catalysis

Article

https://doi.org/10.1038/s41929-024-01147-y

Dinuclear Cu(I) molecular electrocatalyst for CO_2-to-C_3 product conversion

In the format provided by the authors and unedited

This Supplementary Information file includes:
Supplementary Figures 1-23
Supplementary Tables 1-12
Supplementary Methods
Supplementary references 1-33

Supplementary Table 1. Summary of CO_2 electrochemically converted into C_{2+} products using molecular metal complex catalysts.

Catalyst	C_3 product FE (%)	Confirmed C_2 products	*Operando* XAFS measurement	CO_2 adsorption and retaining ability	Ref
CuBr-4PP	**12 % C_3H_7OH**	**C_2H_4, C_2H_5OH**	**○ No decomposition**	**Adsorption and retaining**	**This work**
GMC-[Cu2(NTB)2]	0	C_2H_4	× Decomposition (metallic Cu clusters from TEM)	×	1
Co-corrole	0	C_2H_5OH, CH_3COO^-	×	×	2
CuPc	0	C_2H_4	○ Decomposition (metallic Cu clusters)	×	3
Cu–pyromellic acid	0	CH_3COOH, C_2H_5OH	× Decomsition (Cu-Cu2O metal from XPS, TEM)	Adsorption only	4
[CuII(LNH2)]	0	CH_3COOH,C_2H_5OH	×	×	5
Cu3-Br	0	C_2H_4	×[a]	Adsorption only	6
PorCu	0	C_2H_4	○ Decomposition[b] (metallic Cu clusters)	×	7
Ru(II) polypyridyl carbene	0	C_2H_5OH, CH_3COO^-	×	×	8

a. Measurement: *ex situ* XPS, XRD, *operando* Raman spectroscopy.

b. It has been shown to decompose in another paper (Ref. 3).

All previously reported experiments except those in Ref. 6 were performed using an H-type cell. Those with no description of the molecular catalytic state after the reaction are those for which no detailed analysis was performed.

Supplementary Methods

X-ray single-crystal experiments. Single clear yellowish colourless needle crystals of **CuBr-4PP** recrystallised from a mixture of CH_2Cl_2(DCM) and diethyl ether by cooling. A suitable crystal with dimensions 0.26 × 0.15 × 0.15 mm^3 was selected and mounted on a MITIGEN MicroMount in perfluoroether oil on a Rigaku Saturn724+ (2x2 bin mode) diffractometer. The crystal was kept at a steady T = 123.15 K during data collection. Data were collected using a Rigaku Saturn724+ (2x2 bin mode) diffractometer equipped with a Rigaku CGD-5A low-temperature device operating at T = 123.15 K. Data were measured *w* scans using MoK_a radiation. The maximum resolution that was achieved was Θ = 31.2° (0.69 Å). The unit cell was refined on 4002 reflections, 28% of the observed reflections. Data reduction, scaling and absorption corrections were performed. The final completeness is 84.49% at 0.69 Å or 98.01% at 0.83 Å. Data were collected using CrystalClear-SM 1.4.0 SP1[9] and processed with CrysAlisPro 1.171.39.46[10]. The absorption coefficient *m* of this material is 2.586 mm^{-1} at this wavelength (λ = 0.71075Å) and the minimum and maximum transmissions are 0.640 and 0.764. The structure was solved with the SHELXT[11] solution program using dual SPACE methods and by using Olex2[12] as the graphical interface. The model was refined with SHELXL[13] using full matrix least squares minimisation on $\boldsymbol{F^2}$. All non-hydrogen atoms were refined anisotropically. Hydrogen atom positions were calculated geometrically and refined using the riding model. There is a single molecule in the asymmetric unit, which is represented by the reported sum formula. In other words: Z is 2 and Z' is 1.

A colourless prism-shaped crystal for **CuBr-BisM** recrystallised from a mixture of DCM and diethyl ether by cooling. A suitable crystal with dimensions 0.23 × 0.21 × 0.12 mm^3 was selected and mounted on a Hampton Research Mounted CryoLoop with Paraton-N on the diffractometer. Data were collected using a Rigaku Saturn724+ (2x2 bin mode) diffractometer equipped with a Rigaku CGD-5A low-temperature device operating at T = 123.15 K. Data were measured using *w* scans using Mo K_a radiation. The maximum resolution that was achieved was Θ = 29.130° (0.73 Å). The diffraction pattern was indexed and the total number of runs and images was based on the strategy calculation from the program CrysAlisPro[10]. The unit cell was refined using CrysAlisPro[10] on 38332 reflections, 34% of the observed reflections. Data reduction, scaling and absorption corrections were performed using CrysAlisPro[10]. The final completeness is 99.12 % at 0.73 Å or 99.95% at 0.84 Å. A multi-scan absorption correction was performed using CrysAlisPro[10] Empirical absorption correction using spherical harmonics, implemented in SCALE3 ABSPACK scaling algorithm. The structure was solved and the space group *Pbca* (# 61) determined by the SHELXT[11] structure solution program using dual SPACE methods by using Olex2[12] as the graphical interface. The model was refined with SHELXL[13] using full matrix least squares minimisation on $\boldsymbol{F^2}$. The absorption coefficient *m* of this material is 2.696 mm^{-1} at this wavelength (λ = 0.71073Å) and the minimum and maximum transmissions are 0.900 and 1.000. All non-hydrogen atoms were refined anisotropically. Hydrogen atom positions were calculated geometrically and refined using the riding model. There is a single molecule in the asymmetric unit, which is represented by the reported sum formula. In other words: Z is 8 and Z' is 1. After examining the charge balance of the entire crystal, we attributed a portion of the electron density distribution to Br^- ions. Because disorder was observed among the Br^- ions, they were modeled by dividing them such that the sum of their occupancies was equal to 1. The occupancies were 0.5/0.4/0.1. The disordered structure of the diethyl ether molecular was refined with restrictions (SADI, ISOR) and constrictions (EADP). DFIX and DANG restraint were restraints were used to restrain the bond lengths to chemically reasonable values and SIMU/RIGU restraints were used to

stabilize the refinement of the coordination sphere.

A clear yellowish colourless plate-shaped crystal for **CuBr-12B** recrystallized from a mixture of DCM and diethyl ether by cooling. A suitable crystal with dimensions 0.148 × 0.086 × 0.01 mm^3 was selected and mounted on a Hampton Research Mounted CryoLoop with Paraton-N on the diffractometer. Data were collected using a Rigaku Saturn724+ with AFC10 diffractometer operating at T = 123.15 K. Data were measured using w scans using Mo K_a radiation. The maximum resolution that was achieved was Θ = 30.899° (0.75 Å). The diffraction pattern was indexed and the total number of runs and images was based on the strategy calculation from the program CrysAlisPro.[10] The unit cell was refined using CrysAlisPro[10] on 111962 reflections, 19% of the observed reflections. The final completeness is 99.08 % at 0.75 Å or 99.75 % at 0.83 Å. Data were collected using CrystalClear-SM 1.4.0 SP1[9] and processed with CrysAlisPro 1.171.39.46[10]. The absorption coefficient m of this material is 2.589 mm^{-1} at this wavelength (λ = 0.71073Å). The structure was solved and the space group $P2_1$ (# 4) determined by the SHELXT[11] structure solution program using dual SPACE methods by using Olex2[12] as the graphical interface. The model was refined with SHELXL[13] using full matrix least squares minimisation on $\boldsymbol{F^2}$. The crystal was refined as an inversion twin with a final refined BASF ratio of 0.712 (9) /0.288 (9). All non-hydrogen atoms were refined anisotropically. Hydrogen atom positions were calculated geometrically and refined using the riding model. There is a single molecule in the asymmetric unit, which is represented by the reported sum formula. In other words: Z is 2 and Z' is 1.

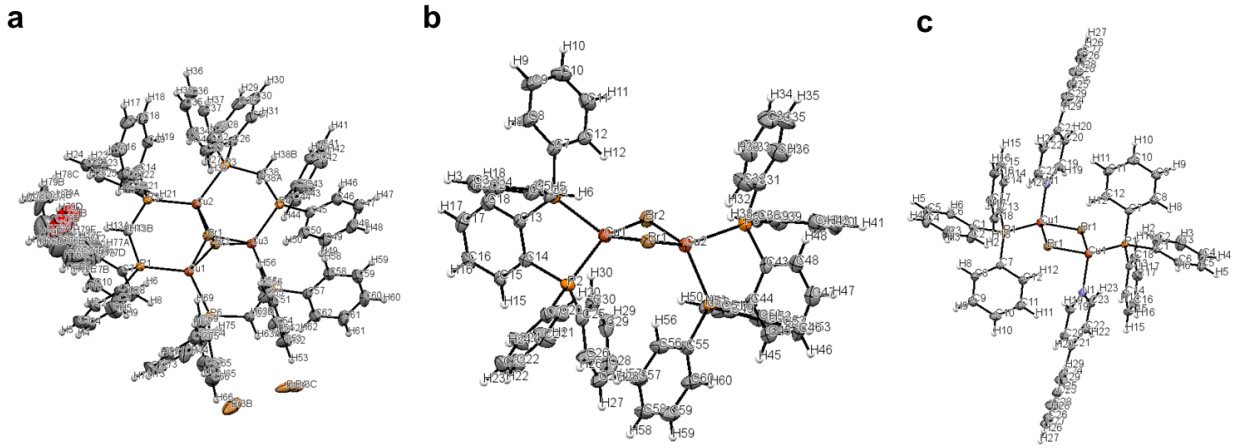

Supplementary Fig. 1. The molecular crystal structure of **a** [$Cu_3(\mu\text{-}Br)_2$(Bis-methyl-bisphenylphosphine)$_3$]Br^- (CuBr-BisM), **b** Cu_2Br_2(1,2-phenyl-bisphenylphosphine)$_2$ (CuBr-12B) and **c** $Cu_2(\mu\text{-}Br)_2$(triphenylphosphine)$_2$(4-phenylpyridine)$_2$ (CuBr-4PP).

Single-crystal X-ray structure analysis and an electron density map for CuBr-BisM revealed a major backbone molecule consisting of a Cu_3Br_2 cluster and a phosphine bidentate ligand, whereas CuBr-12B and CuBr-4PP were found to be Cu dinuclear metal complexes.

Supplementary Table 2. Reflection statistics for CuBr-BisM

Empirical formula	$C_{75}H_{65}Br_{3.01}Cu_3P_{6+}C_4H_{10}O$
Formula weight	1657.35
Temperature of data collection/K	123.15
Wavelength used/Å	0.71073
Crystal system	orthorhombic
Space group	*Pbca*
Unit cell dimensions (including volume)	a = 15.7124(2) Å, b = 25.0060(3) Å, c = 36.9047(5) Å, $\alpha = \beta = \gamma = 90^{\circ}$, V = 14500.0(3) Å^3
Number of molecules per unit cell(Z)	8
Calculated density(r_{calc})/ g cm^{-3}	1.519
Absorption coefficient(m)/ mm^{-1}	2.703
F(000)	6720.0
Crystal size / mm^3	0.227 × 0.214 × 0.117
Radiation	Mo Kα (λ = 0.71073)
Theta range of data collection/ 2Θ_ °	3.254 to 58.26
Index ranges for h, k and l	-21 ≤ h ≤ 20, -34 ≤ k ≤ 34, -49 ≤ l ≤ 43
Total number of collected reflections	106977
Number of independent reflections with merging R-value	19341 [R_{int} = 0.0837, R_{sigma} = 0.0645]
Completeness of the data	0.999
Absorption correction method	multi-scan
Refinement method	Full-matrix least-squares on F^2
Number of unique data used for refinement	19341
Number of restraints	114
Number of refined parameters	879
Goodness of fit on F^2	1.056
Final R indexes [I>=2σ (I)]	R_1 = 0.0577, wR_2 = 0.1234
Final R indexes [all data]	R_1 = 0.0913, wR_2 = 0.1362
Largest diff. peak/hole / e Å^{-3}	1.52/-0.80

Supplementary Table 3. Fractional Atomic Coordinates (×10^4) and Equivalent Isotropic Displacement Parameters (Å^2×10^3) for CuBr-BisM. U_{eq} is defined as 1/3 of the trace of the orthogonalised U_{IJ} tensor.

Atom	***x***	***y***	***z***	U_{eq}
Br1	4718.1(3)	4259.0(2)	5820.2(2)	22.41(9)
Br2	4925.3(2)	4417.9(2)	6824.0(2)	22.21(9)
Cu1	4156.9(3)	4919.7(2)	6317.1(2)	22.30(11)
Cu2	4372.3(3)	3689.5(2)	6379.9(2)	23.33(12)
Cu3	5978.6(3)	4409.9(2)	6264.0(2)	22.60(11)
P1	2731.2(6)	4826.0(4)	6345.4(3)	22.3(2)
P2	2954.3(7)	3603.7(4)	6342.3(3)	22.5(2)
P3	5216.7(7)	2970.0(4)	6453.2(3)	21.3(2)
P4	6791.0(6)	3684.5(4)	6379.4(3)	20.7(2)
P5	6528.4(6)	5234.8(4)	6185.5(3)	21.3(2)
P6	4781.0(7)	5728.2(4)	6298.1(3)	21.5(2)
C1	2127(3)	5271.8(16)	6044.7(12)	27.1(9)
C2	1398(3)	5543.8(19)	6143.8(14)	37.3(11)
C3	959(3)	5848(2)	5890.1(16)	44.9(13)
C4	1237(3)	5883(2)	5538.7(16)	46.4(14)
C5	1958(4)	5618(2)	5440.7(17)	60.4(17)
C6	2406(3)	5318(2)	5689.7(15)	49.1(14)
C7	2211(3)	4918.9(17)	6780.4(12)	28.6(10)
C8	2528(3)	5314.6(19)	7006.0(13)	35.1(11)
C9	2117(3)	5444(2)	7328.8(14)	43.6(13)
C10	1409(4)	5163(2)	7432.0(15)	46.5(13)

C11	1099(3)	4764(2)	7219.1(17)	53.4(15)
C12	1483(3)	4643(2)	6888.0(15)	42.0(12)
C13	2373(3)	4181.1(15)	6164.5(12)	24.2(9)
C14	2691(3)	3069.6(17)	6024.2(12)	27.7(9)
C15	2272(3)	3134(2)	5696.8(13)	39.1(12)
C16	2112(4)	2692(2)	5478.3(15)	52.5(15)
C17	2370(4)	2190(2)	5581.7(15)	47.9(14)
C18	2793(3)	2125.3(19)	5902.3(15)	41.3(12)
C19	2955(3)	2557.8(18)	6121.9(13)	33.3(10)
C20	2367(3)	3391.0(17)	6741.7(12)	27.6(9)
C21	2769(3)	3403(2)	7074.2(13)	36.8(11)
C22	2375(4)	3193(2)	7382.9(14)	45.9(13)
C23	1578(4)	2984(2)	7351.5(15)	45.7(14)
C24	1156(3)	2975.9(19)	7026.6(16)	42.4(13)
C25	1549(3)	3178.5(19)	6717.5(14)	36.7(11)
C26	5429(3)	2538.6(16)	6068.2(12)	24.2(9)
C27	4981(3)	2628.2(18)	5744.5(12)	31.0(10)
C28	5089(4)	2281(2)	5455.7(14)	43.5(13)
C29	5626(4)	1848(2)	5482.4(14)	44.1(13)
C30	6066(3)	1762(2)	5794.8(15)	43.8(13)
C31	5974(3)	2101.7(18)	6088.7(14)	36.0(11)
C32	4806(2)	2508.5(16)	6797.1(11)	23.5(9)
C33	4639(3)	2714.2(18)	7141.4(13)	32.2(10)
C34	4268(3)	2402.2(19)	7408.0(13)	34.6(11)
C35	4054(3)	1876.0(19)	7330.5(14)	35.4(11)
C36	4220(3)	1666.6(18)	6994.7(14)	36.1(11)
C37	4592(3)	1981.7(17)	6728.3(13)	29.8(10)
C38	6265(2)	3149.9(15)	6637.5(11)	22.0(8)
C39	7262(3)	3355.1(17)	5988.9(11)	25.0(9)
C40	7676(3)	2860.3(17)	6009.9(13)	30.2(10)
C41	8023(3)	2632.3(19)	5702.2(14)	37.9(11)
C42	7963(4)	2885(2)	5376.1(14)	49.0(14)
C43	7548(4)	3373(2)	5345.8(14)	51.4(14)
C44	7199(3)	3608(2)	5654.6(13)	40.3(12)
C45	7674(3)	3837.4(16)	6688.8(11)	24.7(9)
C46	8466(3)	3597.9(19)	6675.9(13)	33.3(10)
C47	9078(3)	3727(2)	6929.9(14)	39.9(12)
C48	8905(3)	4090(2)	7199.6(13)	39.3(12)
C49	8125(3)	4336.7(19)	7213.4(14)	37.9(11)
C50	7509(3)	4213.5(18)	6958.0(12)	30.6(10)
C51	6615(3)	5489.4(17)	5723.0(12)	25.8(9)
C52	6894(3)	6005.4(19)	5652.5(13)	36.3(11)
C53	6937(4)	6194(2)	5300.2(13)	44.6(13)
C54	6690(4)	5876(2)	5015.6(14)	44.3(13)
C55	6411(4)	5362(2)	5082.9(14)	45.4(13)
C56	6380(3)	5167.5(19)	5433.0(13)	35.9(11)
C57	7605(3)	5325.3(17)	6357.5(11)	25.4(9)
C58	8235(3)	4966.7(19)	6249.2(14)	36.4(11)
C59	9056(3)	5010(2)	6384.3(15)	43.8(13)
C60	9265(3)	5412(2)	6618.4(15)	46.2(13)
C61	8658(3)	5772(2)	6720.7(15)	47.1(14)
C62	7828(3)	5729.0(19)	6596.2(14)	39.3(12)
C63	5914(2)	5750.1(16)	6422.4(11)	23.0(8)
C64	4710(3)	6102.6(17)	5875.8(12)	28.3(10)
C65	4888(3)	6649.2(19)	5848.3(15)	38.0(11)
C66	4836(3)	6900(2)	5516.7(17)	51.9(15)
C67	4623(4)	6615(3)	5210.0(17)	57.8(17)

C68	4459(4)	6086(2)	5230.3(15)	54.5(15)
C69	4505(3)	5827(2)	5565.5(13)	41.4(12)
C70	4277(3)	6153.6(16)	6635.2(12)	26.1(9)
C71	3538(3)	6428(2)	6548.0(15)	41.6(12)
C72	3061(4)	6686(2)	6812.5(18)	56.2(16)
C73	3311(3)	6671.2(19)	7168.0(16)	46.5(14)
C74	4043(3)	6412(3)	7258.9(16)	54.8(16)
C75	4523(3)	6149(2)	6996.0(14)	45.8(13)
Br3A	7013(3)	7037.4(18)	6779.0(11)	66.8(12)
Br3B	5405(5)	7388(3)	6567(2)	74(2)
Br3C	7273(2)	7030.3(14)	6877.5(8)	38.7(5)
O1A	425(8)	4103(4)	5274(3)	97(3)
C76A	823(10)	4578(6)	5181(4)	159(7)
C77A	1190(20)	4570(11)	4769(6)	196(9)
C78A	25(13)	4187(7)	5606(4)	147(7)
C79A	-149(8)	3607(7)	5784(4)	113(6)
O1B	708(11)	3846(6)	5325(5)	97(3)
C76B	360(20)	4365(10)	5273(9)	159(7)
C77B	820(30)	4608(15)	4892(12)	196(9)
C78B	79(9)	3574(5)	5526(4)	68(5)
C79B	278(9)	3994(5)	5892(4)	65(4)

Supplementary Table 4. Anisotropic Displacement Parameters ($Å^2 \times 10^3$) for CuBr-BisM. The Anisotropic displacement factor exponent takes the form: $-2\pi^2[h^2a^{*2}U_{11}+2hka^*b^*U_{12}+\ldots]$.

Atom	$\mathbf{U_{11}}$	$\mathbf{U_{22}}$	$\mathbf{U_{33}}$	$\mathbf{U_{23}}$	$\mathbf{U_{13}}$	$\mathbf{U_{12}}$
Br1	24.99(19)	24.73(19)	17.5(2)	1.34(15)	-0.71(16)	-2.16(15)
Br2	22.80(19)	24.79(19)	19.1(2)	1.20(15)	-0.56(15)	-0.15(15)
Cu1	19.3(2)	21.5(2)	26.1(3)	2.2(2)	0.0(2)	-0.57(18)
Cu2	19.9(2)	22.7(2)	27.4(3)	3.9(2)	-1.3(2)	0.32(19)
Cu3	21.8(2)	19.9(2)	26.1(3)	1.7(2)	0.3(2)	-0.13(19)
P1	18.2(5)	21.2(5)	27.4(6)	3.5(4)	0.6(4)	1.4(4)
P2	20.4(5)	20.1(5)	27.1(6)	3.1(4)	0.2(4)	-0.1(4)
P3	22.7(5)	20.7(5)	20.6(6)	-0.3(4)	-1.4(4)	-0.8(4)
P4	20.1(5)	22.1(5)	19.8(6)	-1.1(4)	-1.1(4)	-0.1(4)
P5	18.8(5)	20.5(5)	24.4(6)	1.2(4)	0.9(4)	-1.0(4)
P6	20.0(5)	19.8(5)	24.6(6)	2.4(4)	-0.5(4)	0.8(4)
C1	24(2)	21.6(19)	35(3)	6.6(18)	-5.8(18)	-1.0(16)
C2	35(3)	34(2)	43(3)	-1(2)	-2(2)	11(2)
C3	39(3)	36(3)	60(4)	0(2)	-14(3)	14(2)
C4	47(3)	36(3)	56(4)	17(2)	-14(3)	4(2)
C5	65(4)	68(4)	48(4)	33(3)	7(3)	16(3)
C6	41(3)	59(3)	47(3)	27(3)	12(3)	16(3)
C7	24(2)	27(2)	35(3)	8.9(19)	7.0(18)	5.5(17)
C8	39(3)	34(2)	32(3)	3(2)	9(2)	-4(2)
C9	56(3)	38(3)	37(3)	3(2)	11(3)	-4(2)
C10	53(3)	44(3)	43(3)	5(2)	22(3)	10(2)
C11	36(3)	55(3)	69(4)	7(3)	26(3)	-1(3)
C12	31(3)	44(3)	51(3)	-6(2)	14(2)	-3(2)
C13	20.7(19)	20.8(19)	31(2)	2.0(17)	-3.0(17)	-0.9(15)
C14	21(2)	27(2)	35(3)	-1.4(18)	3.3(18)	-4.3(16)
C15	43(3)	36(3)	38(3)	-7(2)	-6(2)	-6(2)
C16	68(4)	53(3)	37(3)	-12(3)	-9(3)	-10(3)
C17	56(3)	40(3)	47(3)	-19(3)	8(3)	-11(2)
C18	35(3)	30(2)	59(4)	-9(2)	9(2)	-3(2)

C19	28(2)	30(2)	42(3)	-4(2)	-3(2)	-1.8(18)
C20	25(2)	24(2)	33(3)	0.1(18)	6.6(18)	2.9(16)
C21	40(3)	40(3)	30(3)	-3(2)	3(2)	-1(2)
C22	60(4)	48(3)	29(3)	0(2)	13(3)	0(3)
C23	60(4)	40(3)	37(3)	1(2)	26(3)	3(2)
C24	29(2)	34(3)	65(4)	7(2)	18(2)	3(2)
C25	27(2)	36(3)	46(3)	10(2)	7(2)	0.0(19)
C26	25(2)	22.3(19)	26(2)	-4.3(16)	3.8(17)	-3.9(16)
C27	37(2)	30(2)	26(3)	1.0(18)	2(2)	-10.6(19)
C28	58(3)	44(3)	28(3)	-4(2)	1(2)	-21(3)
C29	53(3)	40(3)	38(3)	-17(2)	16(3)	-17(2)
C30	31(3)	36(3)	64(4)	-22(3)	9(3)	-6(2)
C31	32(2)	31(2)	45(3)	-10(2)	-3(2)	-1.6(19)
C32	22(2)	26(2)	23(2)	4.9(17)	-4.2(17)	-1.2(16)
C33	33(2)	29(2)	34(3)	0.5(19)	1(2)	-3.7(18)
C34	37(3)	40(3)	27(3)	3(2)	5(2)	-1(2)
C35	30(2)	37(3)	40(3)	15(2)	1(2)	-4.0(19)
C36	39(3)	26(2)	43(3)	7(2)	0(2)	-5.5(19)
C37	31(2)	29(2)	30(3)	-1.2(18)	2.7(19)	-2.9(18)
C38	22.5(19)	21.3(19)	22(2)	-1.6(16)	-2.2(16)	-0.2(15)
C39	23(2)	30(2)	22(2)	-6.2(17)	0.4(17)	0.0(16)
C40	27(2)	30(2)	34(3)	-5.8(19)	1.3(19)	1.6(18)
C41	38(3)	34(2)	42(3)	-13(2)	2(2)	5(2)
C42	58(4)	61(4)	28(3)	-16(3)	10(3)	7(3)
C43	70(4)	56(3)	28(3)	-3(2)	6(3)	10(3)
C44	52(3)	38(3)	31(3)	0(2)	1(2)	10(2)
C45	25(2)	27(2)	22(2)	-1.4(17)	-2.3(17)	-1.9(16)
C46	27(2)	36(2)	37(3)	-4(2)	-6(2)	3.2(18)
C47	24(2)	48(3)	47(3)	0(2)	-8(2)	3(2)
C48	36(3)	47(3)	35(3)	0(2)	-13(2)	-14(2)
C49	39(3)	39(3)	35(3)	-11(2)	-5(2)	-5(2)
C50	29(2)	32(2)	31(3)	-9.0(19)	-4.4(19)	-0.8(18)
C51	22(2)	27(2)	28(2)	2.6(17)	1.1(17)	-3.2(16)
C52	49(3)	32(2)	28(3)	-1(2)	-2(2)	-14(2)
C53	63(4)	36(3)	35(3)	10(2)	4(3)	-14(2)
C54	58(3)	53(3)	22(3)	8(2)	3(2)	-16(3)
C55	61(3)	48(3)	27(3)	-5(2)	3(2)	-19(3)
C56	44(3)	34(2)	29(3)	-2(2)	7(2)	-13(2)
C57	20.5(19)	27(2)	28(2)	2.0(17)	0.9(17)	-1.6(16)
C58	28(2)	35(2)	46(3)	-4(2)	2(2)	0.2(19)
C59	25(2)	46(3)	61(4)	-4(3)	3(2)	7(2)
C60	22(2)	63(4)	53(4)	-1(3)	-5(2)	-1(2)
C61	30(3)	58(3)	53(4)	-14(3)	-10(2)	-7(2)
C62	32(2)	36(3)	50(3)	-10(2)	-6(2)	4(2)
C63	23(2)	22.1(19)	24(2)	2.5(16)	-1.8(17)	0.4(15)
C64	21(2)	27(2)	37(3)	8.0(19)	0.6(18)	2.3(16)
C65	34(3)	32(2)	48(3)	10(2)	-4(2)	-0.8(19)
C66	45(3)	43(3)	68(4)	31(3)	0(3)	-3(2)
C67	58(4)	68(4)	47(4)	34(3)	-3(3)	0(3)
C68	74(4)	58(4)	31(3)	15(3)	-6(3)	-7(3)
C69	55(3)	40(3)	29(3)	6(2)	-8(2)	-1(2)
C70	23(2)	22.3(19)	33(3)	-2.7(17)	3.3(18)	-1.1(16)
C71	37(3)	46(3)	42(3)	5(2)	2(2)	14(2)
C72	55(4)	40(3)	74(5)	13(3)	20(3)	24(3)
C73	49(3)	31(3)	60(4)	-14(2)	24(3)	-5(2)
C74	38(3)	85(5)	42(3)	-23(3)	3(3)	-8(3)
C75	30(3)	75(4)	33(3)	-9(3)	0(2)	7(2)

Br3A	125(4)	28.6(10)	47(2)	-11.6(14)	50.0(18)	-26.5(19)
Br3B	89(5)	68(4)	66(4)	-32(3)	22(4)	-36(4)
Br3C	63.6(11)	23.8(6)	28.7(12)	-2.7(8)	21.3(7)	-6.7(7)
O1A	106(8)	79(8)	105(6)	-31(6)	1(5)	15(6)
C76A	206(18)	140(13)	130(12)	-7(12)	4(12)	-45(12)
C77A	180(30)	219(18)	190(19)	-23(16)	66(14)	-19(18)
C78A	149(15)	222(17)	70(9)	21(11)	20(9)	57(13)
C79A	44(7)	206(16)	88(10)	-35(9)	29(7)	-60(9)
O1B	106(8)	79(8)	105(6)	-31(6)	1(5)	15(6)
C76B	206(18)	140(13)	130(12)	-7(12)	4(12)	-45(12)
C77B	180(30)	219(18)	190(19)	-23(16)	66(14)	-19(18)
C78B	33(8)	30(7)	142(15)	19(8)	18(9)	2(6)
C79B	45(8)	49(8)	102(12)	32(7)	41(8)	20(7)

Supplementary Table 5. Bond Lengths for CuBr-BisM.

Atom	Atom	Length/Å	Atom	Atom	Length/Å
Br1	Cu1	2.6211(6)	C26	C31	1.391(6)
Br1	Cu2	2.5670(6)	C27	C28	1.385(7)
Br1	Cu3	2.5978(6)	C28	C29	1.376(8)
Br2	Cu1	2.5555(6)	C29	C30	1.361(8)
Br2	Cu2	2.5998(6)	C30	C31	1.386(6)
Br2	Cu3	2.6476(6)	C32	C33	1.395(6)
Cu1	P1	2.2547(11)	C32	C37	1.383(6)
Cu1	P6	2.2482(11)	C33	C34	1.385(6)
Cu2	P2	2.2427(11)	C34	C35	1.388(7)
Cu2	P3	2.2519(11)	C35	C36	1.370(7)
Cu3	P4	2.2586(11)	C36	C37	1.389(6)
Cu3	P5	2.2549(11)	C39	C40	1.400(6)
P1	C1	1.837(4)	C39	C44	1.389(6)
P1	C7	1.816(4)	C40	C41	1.383(6)
P1	C13	1.834(4)	C41	C42	1.362(7)
P2	C13	1.831(4)	C42	C43	1.387(8)
P2	C14	1.826(4)	C43	C44	1.394(7)
P2	C20	1.818(4)	C45	C46	1.382(6)
P3	C26	1.815(4)	C45	C50	1.392(6)
P3	C32	1.833(4)	C46	C47	1.381(6)
P3	C38	1.838(4)	C47	C48	1.374(7)
P4	C38	1.838(4)	C48	C49	1.372(7)
P4	C39	1.817(4)	C49	C50	1.386(6)
P4	C45	1.837(4)	C51	C52	1.387(6)
P5	C51	1.827(4)	C51	C56	1.389(6)
P5	C57	1.822(4)	C52	C53	1.385(7)
P5	C63	1.832(4)	C53	C54	1.373(7)
P6	C63	1.839(4)	C54	C55	1.381(7)
P6	C64	1.821(4)	C55	C56	1.381(7)
P6	C70	1.819(4)	C57	C58	1.393(6)
C1	C2	1.382(6)	C57	C62	1.385(6)
C1	C6	1.386(7)	C58	C59	1.388(7)
C2	C3	1.390(7)	C59	C60	1.365(7)
C3	C4	1.372(8)	C60	C61	1.366(7)
C4	C5	1.361(8)	C61	C62	1.387(7)
C5	C6	1.380(7)	C64	C65	1.399(6)
C7	C8	1.385(6)	C64	C69	1.375(7)
C7	C12	1.394(6)	C65	C66	1.378(7)
C8	C9	1.393(7)	C66	C67	1.378(9)
C9	C10	1.369(7)	C67	C68	1.351(8)
C10	C11	1.361(8)	C68	C69	1.399(7)

C11	C12	1.397(7)	C70	C71	1.387(6)
C14	C15	1.385(7)	C70	C75	1.386(7)
C14	C19	1.393(6)	C71	C72	1.389(7)
C15	C16	1.392(7)	C72	C73	1.370(8)
C16	C17	1.372(8)	C73	C74	1.362(8)
C17	C18	1.367(8)	C74	C75	1.394(7)
C18	C19	1.375(6)	O1A	C76A	1.387(11)
C20	C21	1.380(6)	O1A	C78A	1.391(11)
C20	C25	1.394(6)	C76A	C77A	1.627(13)
C21	C22	1.399(7)	C78A	C79A	1.616(12)
C22	C23	1.362(8)	O1B	C76B	1.422(16)
C23	C24	1.370(8)	O1B	C78B	1.412(12)
C24	C25	1.392(7)	C76B	C77B	1.695(17)
C26	C27	1.404(6)	C78B	C79B	1.741(12)

Supplementary Table 6. Bond Angles for CuBr-BisM.

Atom	Atom	Atom	Angle/°	Atom	Atom	Atom	Angle/°
Cu2	Br1	Cu1	73.468(19)	C17	C18	C19	120.4(5)
Cu2	Br1	Cu3	74.607(19)	C18	C19	C14	121.0(5)
Cu3	Br1	Cu1	73.961(18)	C21	C20	P2	118.8(3)
Cu1	Br2	Cu2	74.015(19)	C21	C20	C25	119.1(4)
Cu1	Br2	Cu3	74.202(19)	C25	C20	P2	121.8(4)
Cu2	Br2	Cu3	73.235(18)	C20	C21	C22	120.9(5)
Br2	Cu1	Br1	92.51(2)	C23	C22	C21	118.8(5)
P1	Cu1	Br1	107.52(3)	C22	C23	C24	121.6(5)
P1	Cu1	Br2	112.62(3)	C23	C24	C25	119.8(5)
P6	Cu1	Br1	113.47(3)	C24	C25	C20	119.7(5)
P6	Cu1	Br2	104.97(3)	C27	C26	P3	118.7(3)
P6	Cu1	P1	121.88(4)	C31	C26	P3	122.5(3)
Br1	Cu2	Br2	92.75(2)	C31	C26	C27	118.7(4)
P2	Cu2	Br1	102.33(3)	C28	C27	C26	119.6(5)
P2	Cu2	Br2	115.98(4)	C29	C28	C27	120.9(5)
P2	Cu2	P3	121.08(4)	C30	C29	C28	119.7(5)
P3	Cu2	Br1	114.53(4)	C29	C30	C31	120.9(5)
P3	Cu2	Br2	106.69(3)	C30	C31	C26	120.3(5)
Br1	Cu3	Br2	90.95(2)	C33	C32	P3	117.7(3)
P4	Cu3	Br1	115.66(3)	C37	C32	P3	123.9(3)
P4	Cu3	Br2	102.26(3)	C37	C32	C33	118.2(4)
P5	Cu3	Br1	110.12(3)	C34	C33	C32	121.2(4)
P5	Cu3	Br2	109.44(3)	C33	C34	C35	119.3(4)
P5	Cu3	P4	122.85(4)	C36	C35	C34	120.2(4)
C1	P1	Cu1	114.97(14)	C35	C36	C37	120.2(4)
C7	P1	Cu1	118.33(15)	C32	C37	C36	120.8(4)
C7	P1	C1	102.9(2)	P4	C38	P3	112.9(2)
C7	P1	C13	107.2(2)	C40	C39	P4	123.1(3)
C13	P1	Cu1	112.32(14)	C44	C39	P4	118.0(3)
C13	P1	C1	98.92(19)	C44	C39	C40	118.9(4)
C13	P2	Cu2	116.28(13)	C41	C40	C39	120.1(4)
C14	P2	Cu2	109.55(14)	C42	C41	C40	120.5(5)
C14	P2	C13	103.5(2)	C41	C42	C43	120.7(5)
C20	P2	Cu2	118.81(15)	C42	C43	C44	119.3(5)
C20	P2	C13	105.5(2)	C39	C44	C43	120.4(5)
C20	P2	C14	101.1(2)	C46	C45	P4	124.6(3)
C26	P3	Cu2	119.27(15)	C46	C45	C50	119.0(4)
C26	P3	C32	103.45(19)	C50	C45	P4	116.4(3)
C26	P3	C38	105.71(19)	C47	C46	C45	120.1(4)
C32	P3	Cu2	112.25(14)	C48	C47	C46	120.6(5)

C32	P3	C38	102.34(18)	C49	C48	C47	120.0(4)
C38	P3	Cu2	112.14(13)	C48	C49	C50	119.9(5)
C38	P4	Cu3	115.32(13)	C49	C50	C45	120.4(4)
C39	P4	Cu3	116.40(15)	C52	C51	P5	121.5(3)
C39	P4	C38	105.34(19)	C52	C51	C56	118.6(4)
C39	P4	C45	106.26(19)	C56	C51	P5	119.9(3)
C45	P4	Cu3	112.12(14)	C53	C52	C51	120.5(4)
C45	P4	C38	99.71(19)	C54	C53	C52	120.5(5)
C51	P5	Cu3	117.88(14)	C53	C54	C55	119.4(5)
C51	P5	C63	103.88(19)	C56	C55	C54	120.5(5)
C57	P5	Cu3	115.14(14)	C55	C56	C51	120.5(4)
C57	P5	C51	102.29(19)	C58	C57	P5	118.6(3)
C57	P5	C63	103.63(19)	C62	C57	P5	123.2(3)
C63	P5	Cu3	112.35(14)	C62	C57	C58	118.2(4)
C63	P6	Cu1	116.18(13)	C59	C58	C57	120.5(5)
C64	P6	Cu1	117.53(15)	C60	C59	C58	120.5(5)
C64	P6	C63	104.93(19)	C59	C60	C61	119.5(5)
C70	P6	Cu1	108.35(14)	C60	C61	C62	120.9(5)
C70	P6	C63	103.49(19)	C57	C62	C61	120.3(5)
C70	P6	C64	104.9(2)	P5	C63	P6	111.7(2)
C2	C1	P1	124.5(4)	C65	C64	P6	123.5(4)
C2	C1	C6	118.1(4)	C69	C64	P6	118.0(3)
C6	C1	P1	117.3(3)	C69	C64	C65	118.5(4)
C1	C2	C3	120.2(5)	C66	C65	C64	119.8(5)
C4	C3	C2	120.9(5)	C65	C66	C67	120.6(5)
C5	C4	C3	119.0(5)	C68	C67	C66	120.4(5)
C4	C5	C6	120.9(6)	C67	C68	C69	119.6(6)
C5	C6	C1	120.9(5)	C64	C69	C68	121.0(5)
C8	C7	P1	117.4(3)	C71	C70	P6	119.7(4)
C8	C7	C12	118.5(4)	C75	C70	P6	122.1(3)
C12	C7	P1	123.9(4)	C75	C70	C71	117.4(4)
C7	C8	C9	120.9(4)	C70	C71	C72	121.2(5)
C10	C9	C8	119.7(5)	C73	C72	C71	120.4(5)
C11	C10	C9	120.4(5)	C74	C73	C72	119.4(5)
C10	C11	C12	120.6(5)	C73	C74	C75	120.6(5)
C7	C12	C11	119.8(5)	C70	C75	C74	120.9(5)
P2	C13	P1	114.2(2)	C76A	O1A	C78A	107.1(14)
C15	C14	P2	125.7(3)	O1A	C76A	C77A	112.5(13)
C15	C14	C19	118.3(4)	O1A	C78A	C79A	107.4(12)
C19	C14	P2	116.0(3)	C78B	O1B	C76B	104.0(17)
C14	C15	C16	119.9(5)	O1B	C76B	C77B	105.8(17)
C17	C16	C15	120.8(5)	O1B	C78B	C79B	89.4(10)
C18	C17	C16	119.6(5)				

Supplementary Table 7. Torsion Angles for CuBr-BisM.

A	**B**	**C**	**D**	**Angle/°**	**A**	**B**	**C**	**D**	**Angle/°**
Cu1	P1	C1	C2	-136.9(4)	C22	C23	C24	C25	1.0(8)
Cu1	P1	C1	C6	46.0(4)	C23	C24	C25	C20	-0.4(7)
Cu1	P1	C7	C8	37.3(4)	C25	C20	C21	C22	1.8(7)
Cu1	P1	C7	C12	-147.3(4)	C26	P3	C32	C33	175.2(3)
Cu1	P1	C13	P2	49.0(3)	C26	P3	C32	C37	-9.8(4)
Cu1	P6	C63	P5	48.6(3)	C26	P3	C38	P4	79.5(2)
Cu1	P6	C64	C65	164.7(3)	C26	C27	C28	C29	0.3(7)
Cu1	P6	C64	C69	-18.2(4)	C27	C26	C31	C30	-0.4(6)
Cu1	P6	C70	C71	-85.2(4)	C27	C28	C29	C30	-0.9(7)
Cu1	P6	C70	C75	84.1(4)	C28	C29	C30	C31	0.7(8)
Cu2	P2	C13	P1	-43.5(3)	C29	C30	C31	C26	-0.1(7)

Cu2	P2	C14	C15	-114.7(4)	C31	C26	C27	C28	0.3(6)
Cu2	P2	C14	C19	64.0(4)	C32	P3	C26	C27	118.1(3)
Cu2	P2	C20	C21	14.4(4)	C32	P3	C26	C31	-57.5(4)
Cu2	P2	C20	C25	-160.7(3)	C32	P3	C38	P4	-172.5(2)
Cu2	P3	C26	C27	-7.4(4)	C32	C33	C34	C35	-0.3(7)
Cu2	P3	C26	C31	177.0(3)	C33	C32	C37	C36	0.1(6)
Cu2	P3	C32	C33	-54.9(4)	C33	C34	C35	C36	0.8(7)
Cu2	P3	C32	C37	120.0(3)	C34	C35	C36	C37	-0.9(7)
Cu2	P3	C38	P4	-52.0(2)	C35	C36	C37	C32	0.5(7)
Cu3	P4	C38	P3	49.0(2)	C37	C32	C33	C34	-0.2(7)
Cu3	P4	C39	C40	-170.5(3)	C38	P3	C26	C27	-134.7(3)
Cu3	P4	C39	C44	9.0(4)	C38	P3	C26	C31	49.6(4)
Cu3	P4	C45	C46	-146.6(4)	C38	P3	C32	C33	65.5(4)
Cu3	P4	C45	C50	34.9(4)	C38	P3	C32	C37	-119.6(4)
Cu3	P5	C51	C52	175.7(3)	C38	P4	C39	C40	-41.3(4)
Cu3	P5	C51	C56	-2.7(4)	C38	P4	C39	C44	138.2(4)
Cu3	P5	C57	C58	52.5(4)	C38	P4	C45	C46	90.8(4)
Cu3	P5	C57	C62	-126.4(4)	C38	P4	C45	C50	-87.6(4)
Cu3	P5	C63	P6	-53.9(2)	C39	P4	C38	P3	-80.8(2)
P1	C1	C2	C3	-176.3(4)	C39	P4	C45	C46	-18.4(4)
P1	C1	C6	C5	175.9(5)	C39	P4	C45	C50	163.2(3)
P1	C7	C8	C9	174.1(4)	C39	C40	C41	C42	-0.2(7)
P1	C7	C12	C11	-176.1(4)	C40	C39	C44	C43	-0.4(7)
P2	C14	C15	C16	179.9(4)	C40	C41	C42	C43	-0.5(8)
P2	C14	C19	C18	-179.9(4)	C41	C42	C43	C44	0.8(9)
P2	C20	C21	C22	-173.4(4)	C42	C43	C44	C39	-0.3(9)
P2	C20	C25	C24	174.1(4)	C44	C39	C40	C41	0.7(7)
P3	C26	C27	C28	-175.5(3)	C45	P4	C38	P3	169.3(2)
P3	C26	C31	C30	175.2(4)	C45	P4	C39	C40	63.9(4)
P3	C32	C33	C34	175.1(4)	C45	P4	C39	C44	-116.6(4)
P3	C32	C37	C36	-174.8(3)	C45	C46	C47	C48	0.6(8)
P4	C39	C40	C41	-179.8(3)	C46	C45	C50	C49	-1.3(7)
P4	C39	C44	C43	-179.9(4)	C46	C47	C48	C49	-1.5(8)
P4	C45	C46	C47	-177.6(4)	C47	C48	C49	C50	0.9(8)
P4	C45	C50	C49	177.2(4)	C48	C49	C50	C45	0.5(7)
P5	C51	C52	C53	-178.6(4)	C50	C45	C46	C47	0.8(7)
P5	C51	C56	C55	177.5(4)	C51	P5	C57	C58	-76.6(4)
P5	C57	C58	C59	-177.6(4)	C51	P5	C57	C62	104.5(4)
P5	C57	C62	C61	179.2(4)	C51	P5	C63	P6	74.6(2)
P6	C64	C65	C66	178.6(4)	C51	C52	C53	C54	1.1(8)
P6	C64	C69	C68	-178.5(4)	C52	C51	C56	C55	-1.0(7)
P6	C70	C71	C72	169.5(4)	C52	C53	C54	C55	-1.0(9)
P6	C70	C75	C74	-169.7(4)	C53	C54	C55	C56	0.0(9)
C1	P1	C7	C8	-90.8(4)	C54	C55	C56	C51	1.0(8)
C1	P1	C7	C12	84.6(4)	C56	C51	C52	C53	-0.1(7)
C1	P1	C13	P2	170.8(2)	C57	P5	C51	C52	-56.9(4)
C1	C2	C3	C4	0.1(8)	C57	P5	C51	C56	124.7(4)
C2	C1	C6	C5	-1.3(8)	C57	P5	C63	P6	-178.8(2)
C2	C3	C4	C5	-0.4(8)	C57	C58	C59	C60	-1.6(8)
C3	C4	C5	C6	-0.2(9)	C58	C57	C62	C61	0.3(7)
C4	C5	C6	C1	1.0(10)	C58	C59	C60	C61	0.2(9)
C6	C1	C2	C3	0.8(7)	C59	C60	C61	C62	1.4(9)
C7	P1	C1	C2	-6.8(4)	C60	C61	C62	C57	-1.7(9)
C7	P1	C1	C6	176.1(4)	C62	C57	C58	C59	1.3(7)
C7	P1	C13	P2	-82.6(3)	C63	P5	C51	C52	50.7(4)
C7	C8	C9	C10	2.4(8)	C63	P5	C51	C56	-127.7(4)
C8	C7	C12	C11	-0.8(7)	C63	P5	C57	C58	175.6(4)

C8	C9	C10	C11	-0.8(8)	C63	P5	C57	C62	-3.3(4)
C9	C10	C11	C12	-1.6(9)	C63	P6	C64	C65	-64.5(4)
C10	C11	C12	C7	2.4(8)	C63	P6	C64	C69	112.6(4)
C12	C7	C8	C9	-1.6(7)	C63	P6	C70	C71	150.9(4)
C13	P1	C1	C2	103.3(4)	C63	P6	C70	C75	-39.8(4)
C13	P1	C1	C6	-73.8(4)	C64	P6	C63	P5	-83.0(2)
C13	P1	C7	C8	165.5(3)	C64	P6	C70	C71	41.2(4)
C13	P1	C7	C12	-19.1(4)	C64	P6	C70	C75	-149.6(4)
C13	P2	C14	C15	10.0(4)	C64	C65	C66	C67	-1.1(8)
C13	P2	C14	C19	-171.3(3)	C65	C64	C69	C68	-1.2(8)
C13	P2	C20	C21	-118.3(4)	C65	C66	C67	C68	0.2(9)
C13	P2	C20	C25	66.7(4)	C66	C67	C68	C69	0.1(10)
C14	P2	C13	P1	-163.7(2)	C67	C68	C69	C64	0.4(9)
C14	P2	C20	C21	134.2(4)	C69	C64	C65	C66	1.6(7)
C14	P2	C20	C25	-40.9(4)	C70	P6	C63	P5	167.2(2)
C14	C15	C16	C17	-0.5(8)	C70	P6	C64	C65	44.3(4)
C15	C14	C19	C18	-1.0(7)	C70	P6	C64	C69	-138.6(4)
C15	C16	C17	C18	-0.3(9)	C70	C71	C72	C73	-0.4(9)
C16	C17	C18	C19	0.5(8)	C71	C70	C75	C74	-0.2(8)
C17	C18	C19	C14	0.2(7)	C71	C72	C73	C74	1.5(9)
C19	C14	C15	C16	1.2(7)	C72	C73	C74	C75	-2.0(9)
C20	P2	C13	P1	90.5(3)	C73	C74	C75	C70	1.4(9)
C20	P2	C14	C15	119.1(4)	C75	C70	C71	C72	-0.3(8)
C20	P2	C14	C19	-62.2(4)	C76A	O1A	C78A	C79A	-160.4(13)
C20	C21	C22	C23	-1.3(8)	C78A	O1A	C76A	C77A	-171.0(18)
C21	C20	C25	C24	-0.9(7)	C76B	O1B	C78B	C79B	-67(2)
C21	C22	C23	C24	-0.1(8)	C78B	O1B	C76B	C77B	-155(3)

Supplementary Table 8. Hydrogen Atom Coordinates (Å×10^4) and Isotropic Displacement Parameters (Å^2×10^3) for CuBr-BisM.

Atom	***x***	***y***	***z***	U_{eq}
H2	1196.6	5522.91	6386.06	45
H3	458.78	6033.83	5961.12	54
H4	932.06	6090.21	5366.26	56
H5	2154.12	5639.72	5197.74	73
H6	2912.55	5140.43	5616.83	59
H8	3031.37	5500.32	6939.58	42
H9	2327.52	5725.12	7476.73	52
H10	1133.38	5247.89	7653.74	56
H11	615.28	4566.49	7296.34	64
H12	1249.7	4372.52	6736.68	50
H13A	1760.66	4136.55	6220.91	29
H13B	2432.16	4186.67	5897.47	29
H15	2094.8	3479.94	5621.52	47
H16	1819.95	2737.8	5255	63
H17	2255.02	1890.44	5431.51	57
H18	2976.34	1779.07	5973.83	50
H19	3251.96	2506.75	6343.51	40
H21	3319.65	3556.94	7093.77	44
H22	2658.2	3195.96	7610.31	55
H23	1307.67	2839.42	7560.01	55
H24	597.21	2832.69	7012.18	51
H25	1261.05	3171.92	6491.28	44
H27	4607.2	2924.96	5723.65	37
H28	4789.03	2342.52	5236.22	52
H29	5688.89	1609.3	5283.67	53
H30	6441.12	1464.72	5811.54	53

H31	6284.87	2036.09	6304.98	43
H33	4783.47	3074.91	7193.76	39
H34	4160.52	2546.9	7641.64	41
H35	3792.11	1660.37	7510.67	43
H36	4080.24	1304.67	6944	43
H37	4700.02	1833.52	6495.85	36
H38A	6196.21	3267.12	6892.06	26
H38B	6633.92	2828.92	6637.11	26
H40	7718.67	2680.83	6236.1	36
H41	8304.83	2297.16	5718.2	45
H42	8207.59	2725.29	5167.04	59
H43	7502.16	3544.75	5117.15	62
H44	6916.91	3942.38	5636.35	48
H46	8589.42	3343.73	6491.98	40
H47	9622.95	3563.71	6917.98	48
H48	9325.52	4170.65	7376.42	47
H49	8008.17	4591.39	7397.75	45
H50	6971.38	4386.69	6966.66	37
H52	7056.54	6231.32	5847.55	44
H53	7138.02	6545.92	5254.99	54
H54	6711.48	6008.16	4774.5	53
H55	6239.9	5139.76	4887.09	55
H56	6195.68	4811.21	5475.85	43
H58	8100.69	4690.79	6081.78	44
H59	9476.59	4757.65	6313.39	53
H60	9828.85	5440.55	6709.46	55
H61	8806.29	6056.57	6879.27	57
H62	7410.07	5977.55	6675.19	47
H63A	6148.1	6106.71	6361.9	28
H63B	5971.24	5697.78	6687.19	28
H65	5045.46	6846.9	6057.72	46
H66	4947.9	7272.12	5499.16	62
H67	4590.67	6792.85	4982.83	69
H68	4312.61	5891.15	5018.21	65
H69	4393.01	5453.72	5579.09	50
H71	3353.89	6439.46	6302.89	50
H72	2557.9	6872.85	6746.51	67
H73	2977.24	6840.39	7349.37	56
H74	4228.93	6411.29	7503.91	66
H75	5025.31	5963.67	7065.03	55
H76A	1296.99	4645.45	5351.36	190
H76B	411.51	4875.58	5204.53	190
H77A	1800.48	4478.19	4774.18	294
H77B	1120.39	4923.19	4658.92	294
H77C	884.88	4302.43	4626.2	294
H78A	-518.32	4380	5570.03	176
H78B	393.61	4403.26	5766.54	176
H79A	314.79	3518.03	5950.93	169
H79B	-179.96	3336.59	5592.38	169
H79C	-688.91	3614.8	5917.27	169
H76C	489.03	4597.93	5483.28	190
H76D	-266.41	4345.36	5243.72	190
H77D	1399.47	4465.01	4870.75	294
H77E	843.81	4999.03	4904.61	294
H77F	486.09	4499.56	4680.31	294
H78C	217.61	3193.68	5573.11	82
H78D	-501.57	3610.28	5424.72	82

H79D	381.15	3777.99	6109.61	98
H79E	-214.59	4226.33	5932.35	98
H79F	780.9	4213.23	5841.1	98

Supplementary Table 9. Atomic Occupancy for CuBr-BisM

Atom	***Occupancy***	**Atom**	***Occupancy***	**Atom**	***Occupancy***
Br3A	0.4	Br3B	0.1	Br3C	0.5
O1A	0.6	C76A	0.6	H76A	0.6
H76B	0.6	C77A	0.6	H77A	0.6
H77B	0.6	H77C	0.6	C78A	0.6
H78A	0.6	H78B	0.6	C79A	0.6
H79A	0.6	H79B	0.6	H79C	0.6
O1B	0.4	C76B	0.4	H76C	0.4
H76D	0.4	C77B	0.4	H77D	0.4
H77E	0.4	H77F	0.4	C78B	0.4
H78C	0.4	H78D	0.4	C79B	0.4
H79D	0.4	H79E	0.4	H79F	0.4

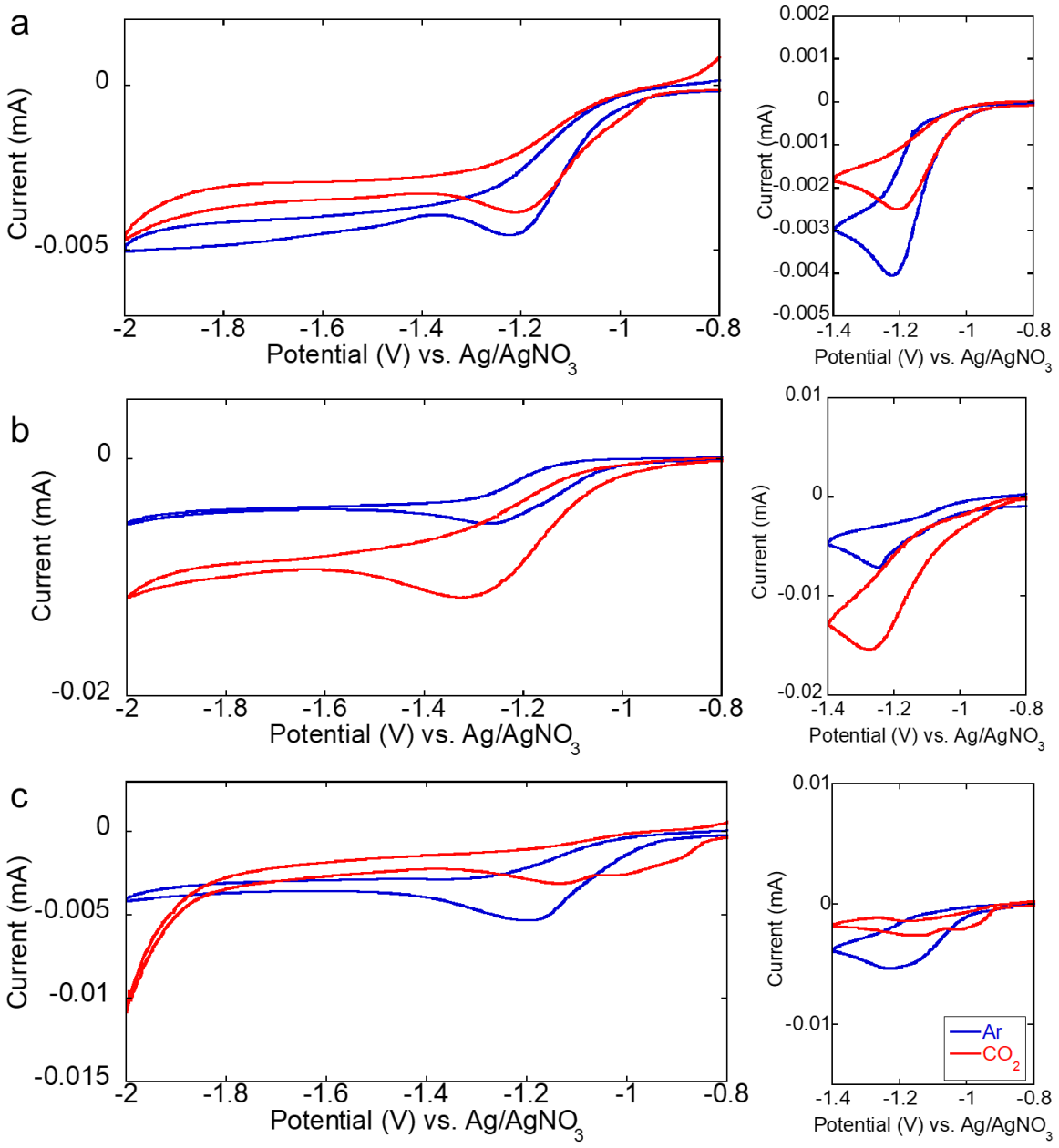

Supplementary Fig. 2. a–c, Cyclic voltammograms of CuBr-BisM, CuBr-12B, and CuBr-4PP, respectively, in MeCN solution containing 0.1 M $NEt_4^+BF_4^-$ under Ar (blue) or CO_2 (red). Measurements were carried out using a glassy carbon working electrode, a Pt counter electrode, and an Ag/AgCl reference electrode. Scan rate: 25 mV s^{-1}.

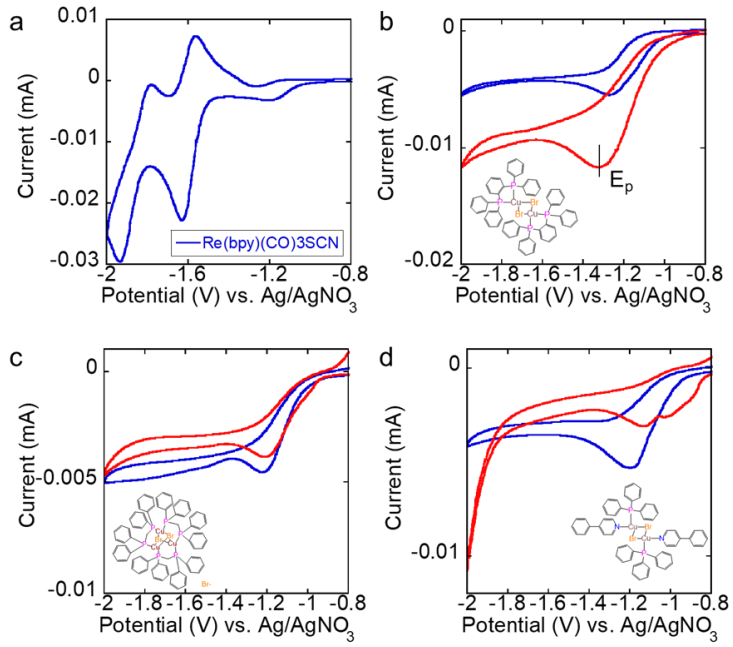

e

Catalysts	Gas	E_p (V vs Ag/$AgNO_3$)	n
CuBr-12B	Ar	-1.26	1.0
	CO_2	-1.31	1.9
CuBr-BisM	Ar	-1.23	0.8
	CO_2	-1.21	0.9
CuBr-4PP	Ar	-1.20	0.8
	CO_2	-1.03	0.4
	CO_2	-1.19	0.5

Supplementary Fig. 3. Cyclic voltammograms for **a** Re(bpy)$(CO)_3$SCN, **b** CuBr-12B, **c** CuBr-BisM and **d** CuBr-4PP, respectively, measured in acetonitrile (MeCN) solution containing 0.1 M $NEt_4^+BF_4^-$ under Ar (blue) or CO_2 (red). The measurements were conducted in the voltage range from −0.8 to −2.0 V using a glassy carbon working electrode, a Pt counter electrode, and an Ag/$AgNO_3$ reference electrode. Scan rate: 25 mV s^{-1}. **f** Estimated number of electrons (n) for each reduction waves.

For irreversible CV curves, it is known that the number of electrons can be estimated from the following equation.[14]

$$i_p(irr) = (2.99 \times 10^5)n(\frac{47.7}{|E_p - E_{p/2}|})^{1/2} AD^{1/2}v^{1/2}C \cdots(1)$$

where i_p, n, A, D, v and C are the peak current (A), number of electrons consumed in the redox reaction, surface area (cm^2) of electrode, diffusion constant (cm^2 s^{-1}) in the solvent, a voltage sweep rate (V s^{-1}), and the bulk concentration (M) of an electroactive species, respectively. E_p, $E_{p/2}$ are the peak potential (mV) of an irreversible wave and the potential (mV) at $i_p/2$, respectively. Using the approximate D obtained from the CV under the same conditions for the reference molecule, for which the number of electrons is already known, the approximate number of reacting electrons can be estimated from Supplementary Equation 1. As a refence, Re(bpy)$(CO)_3$SCN metal complex is reported to have a single-electron reduction wave at −1.6 V vs. Ag/$AgNO_3$.[15] For CV curve reversible molecules, the diffusion constant of an electroactive species can be estimated from the following equation.

$$i_p = (2.69 \times 10^5)n^{3/2}AD^{1/2}v^{1/2}C \cdots(2)$$

From the CV of the Re(bpy)$(CO)_3$SCN (Supplementary Fig. 3a) and Supplementary Eq. 2, the diffusion coefficient in MeCN was estimated to be 1.63×10^{-5} cm^2 s^{-1}. Using this value, the number of reaction electrons for CuBr molecular (Supplemental Fig. 3f) was estimated from Eq. 1.

By the above methods, the number of reaction electrons for each reduction waves were shown in Supplementary Fig. 3f. From these results, the first reduction wave of CuBr-12B was estimated to be a one-electron reduced wave under the Ar atmosphere and a two-electron reduced wave under the CO_2 atmosphere. That of CuBr-BisM was one-electron reduction under both Ar and CO_2 atmospheres. That of CuBr-4PP under Ar was also one-electron reduction. Under CO_2, since a new peak was observed at a lower potential, we have estimated the total electron numbers from

each of the two peaks. The number of electrons at −1.0 V and −1.1 V vs. $Ag/AgNO_3$ were 0.4 and 0.5, respectively. Thus, the coexistence of CO_2 would cause about 40% of the CuBr-4PP to undergo one-electron reduction at lower potentials than that under-Ar atmosphere.

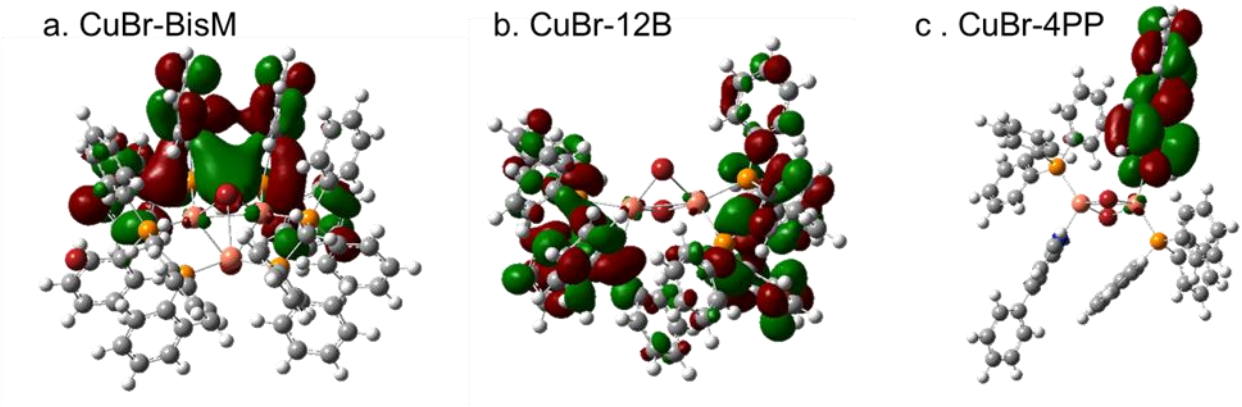

Supplementary Fig. 4. a–c, DFT calculation structure for the lowest unoccupied molecular orbitals (LUMOs) of CuBr-BisM (Supplementary Data 1), CuBr-12B (Supplementary Data 1), and CuBr-4PP (Supplementary Data 1), respectively.

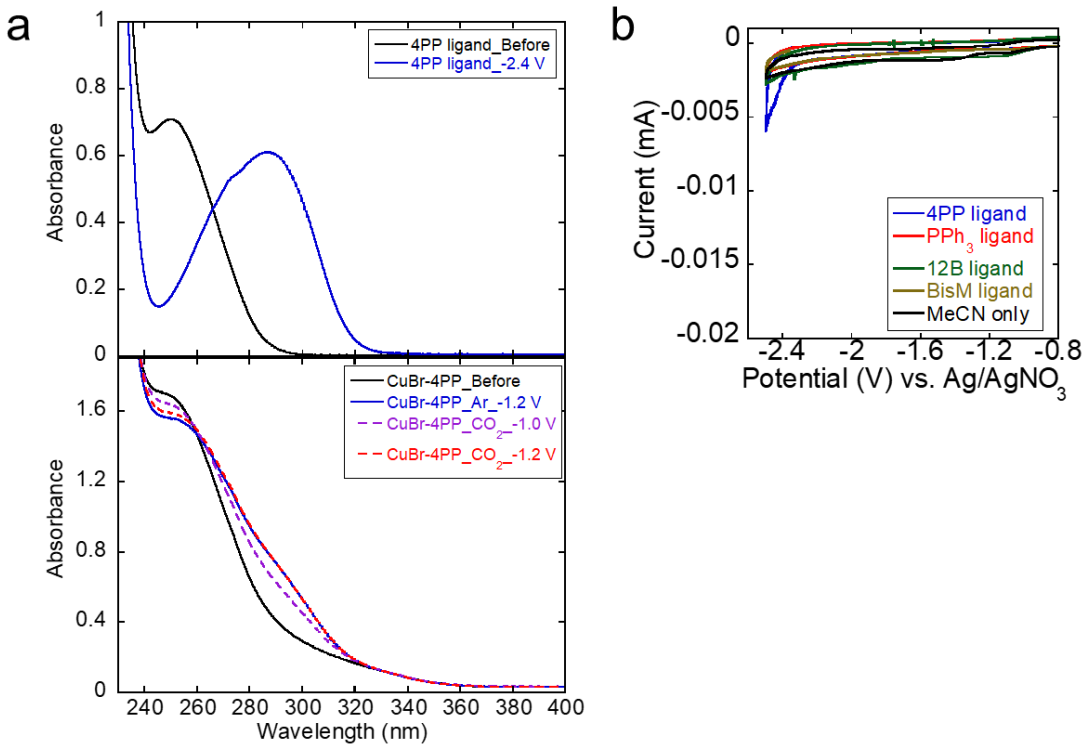

Supplementary Fig. 5. a *In situ* UV spectra for 4PP ligand only under the Ar atmosphere and CuBr-4PP under the Ar or CO_2 atmosphere in MeCN solution containing 0.1 M $NEt_4^+BF_4^-$. **b** Cyclic voltammograms for 0.5 mM ligands alone, measured in acetonitrile (MeCN) solution containing 0.1 M $NEt_4^+BF_4^-$ under Ar. The measurements were conducted in the voltage range from −0.8 to −2.5 V using a glassy carbon working electrode, a Pt counter electrode, and an $Ag/AgNO_3$ reference electrode. Scan rate: 25 mV s^{-1}.

To attribute the reduction wave in MeCN at −1.2 V vs. $Ag/AgNO_3$, a constant potential electrolysis was performed using a two-chamber cell to accumulate reducing species, and the UV-Vis absorption spectrum of the solution was measured. As shown in Supplementary Fig. 5a, under both Ar and CO_2, a new absorption band was observed between 270 and 320 nm and the absorbance around 250 nm decreased compared to before electrolysis. Since the 4PP ligand exhibited a reduction wave at −2.4 V vs. $Ag/AgNO_3$ (Supplementary Fig. 5b), we performed a constant potential electrolysis at this potential and then UV-Vis absorption measurement. As shown in Supplementary Fig. 5a, the spectrum before electrolysis showed a peak at 250 nm, but the peak shifted to 290 nm after electrolysis. This change corresponds well with the change in the absorption spectrum of CuBr-4PP, indicating that the one electron injected at −1.2 V vs. $Ag/AgNO_3$ into CuBr-4PP was accumulated in a 4PP ligand. During the reaction process, the oxidation state of Cu is maintained at +1 during the reaction process, probably due to the sequential electron accumulation to 4PP and proton donation to substrate.

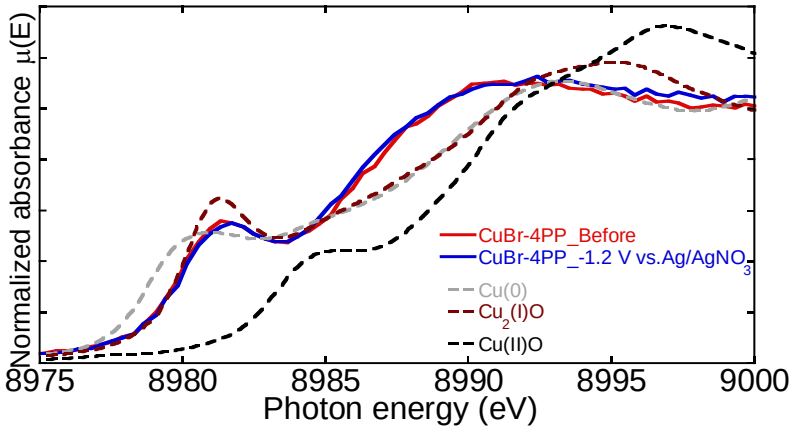

Supplementary Fig. 6, *Operando* Cu-K edge XANES spectra for CuBr-4PP at −1.2 V vs. $Ag/AgNO_3$ in MeCN solution containing 0.1 M $NEt_4^+BF_4^-$ under the CO_2 atmosphere. *Operando* XANES spectra recorded approximately every 5 min. In the figure, "Before" shows the state of molecules dissolved in the electrolyte before the reaction, "−1.2 V vs. $Ag/AgNO_3$" shows the spectrum recorded from 5 to 10 minutes after the reaction begin. The spectra for Cu, $Cu_2(I)O$, and Cu(II)O are also shown for reference.

Charge density analysis of the one-electron reduced species of CuBr-4PP and the initial state of CuBr-4PP showed that the two Cu centers of CuBr-4PP had charge densities of 0.350 and 0.272, whereas those of the one-electron reduced species were 0.375 and 0.205. The decrease in charge density of one Cu center was attributed to electron accumulation in the adjacent phenylpyridine, suggesting that both Cu centers remain in the Cu(I) valent state.

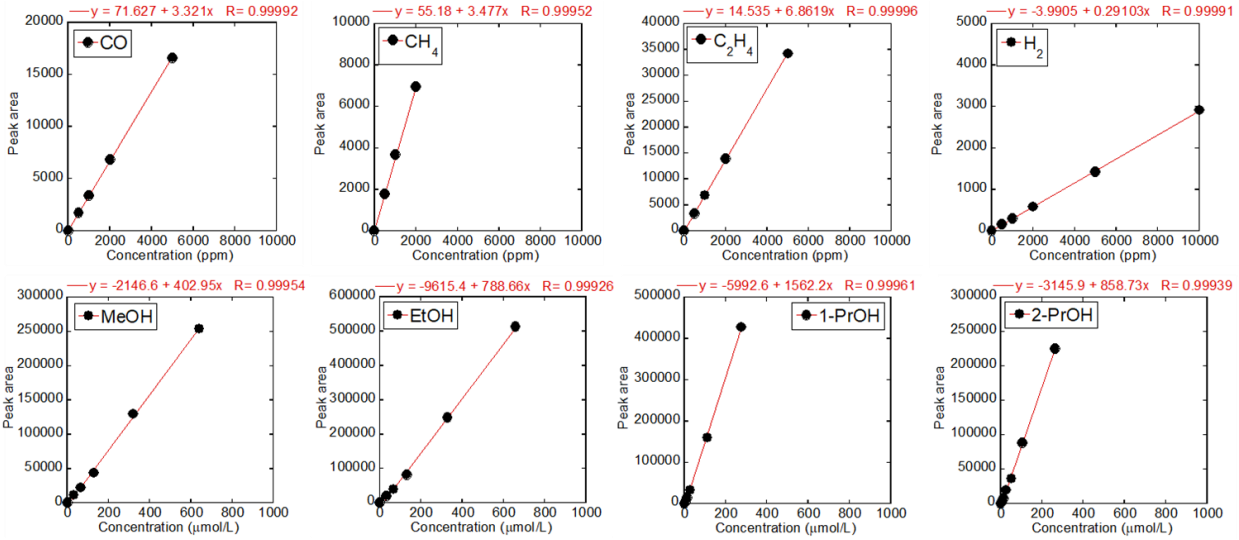

Supplementary Fig. 7. Calibration curves for gas chromatography analysis were prepared to verify the linear response of the instrument. All calibration curves have linearity with high values above R=0.999. The highest measured value for each gas component was within the calibration curve. Alcohol analysis was performed on samples that have been diluted to within the concentration range of the calibration curve and heated in a headspace sampler.

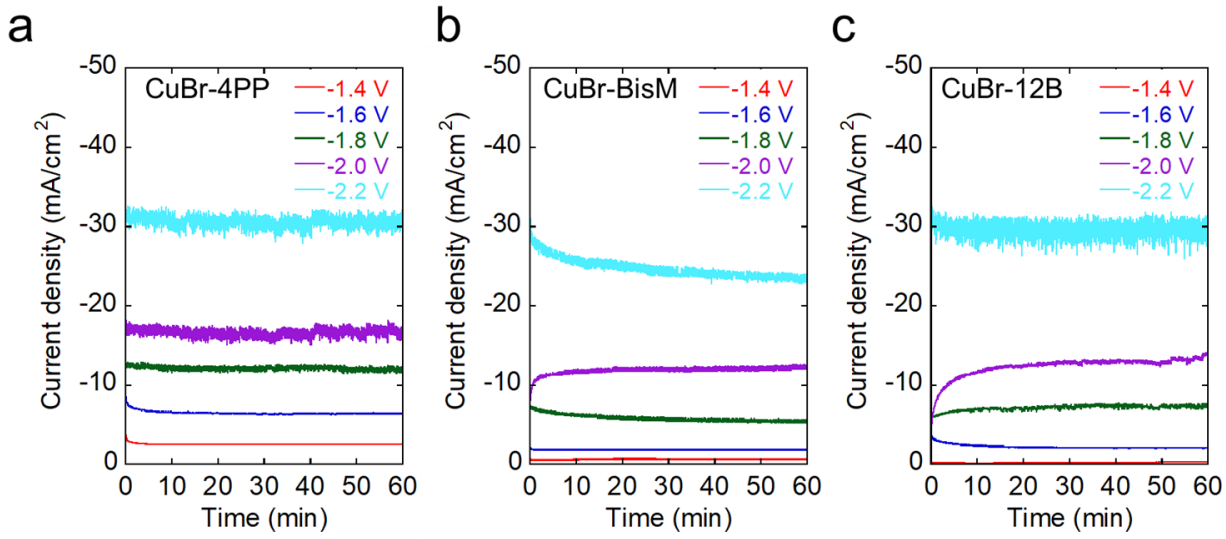

Supplementary Fig. 8. a–c, The time course of the current density using CuBr-4PP, CuBr-BisM, and CuBr-12B electrodes, respectively, in 0.5 M $KHCO_3$ electrolyte.

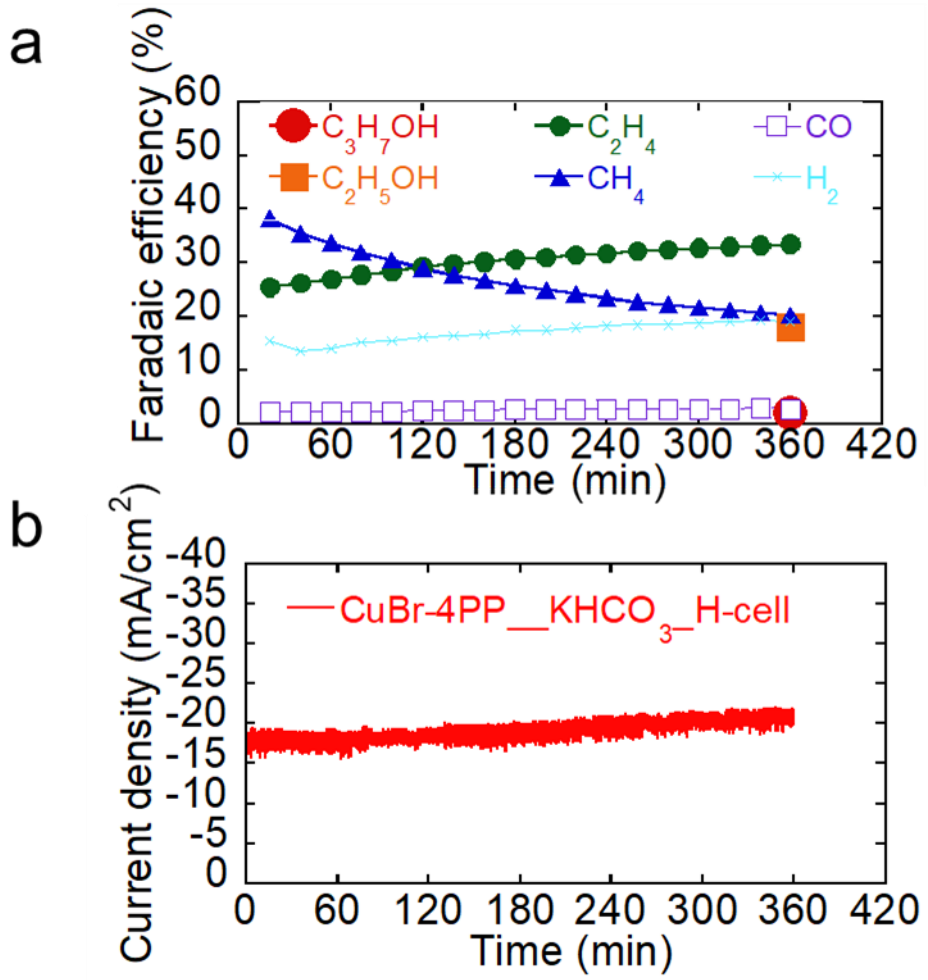

Supplementary Fig. 9. a, Faradaic efficiency of various reduction products observed after CO_2 reduction for 6 h using the CuBr-4PP electrodes at −2.0 V vs. Ag/AgCl in 0.5 M $KHCO_3$ electrolyte in a H-type cell. **b**, The time course of the current density.

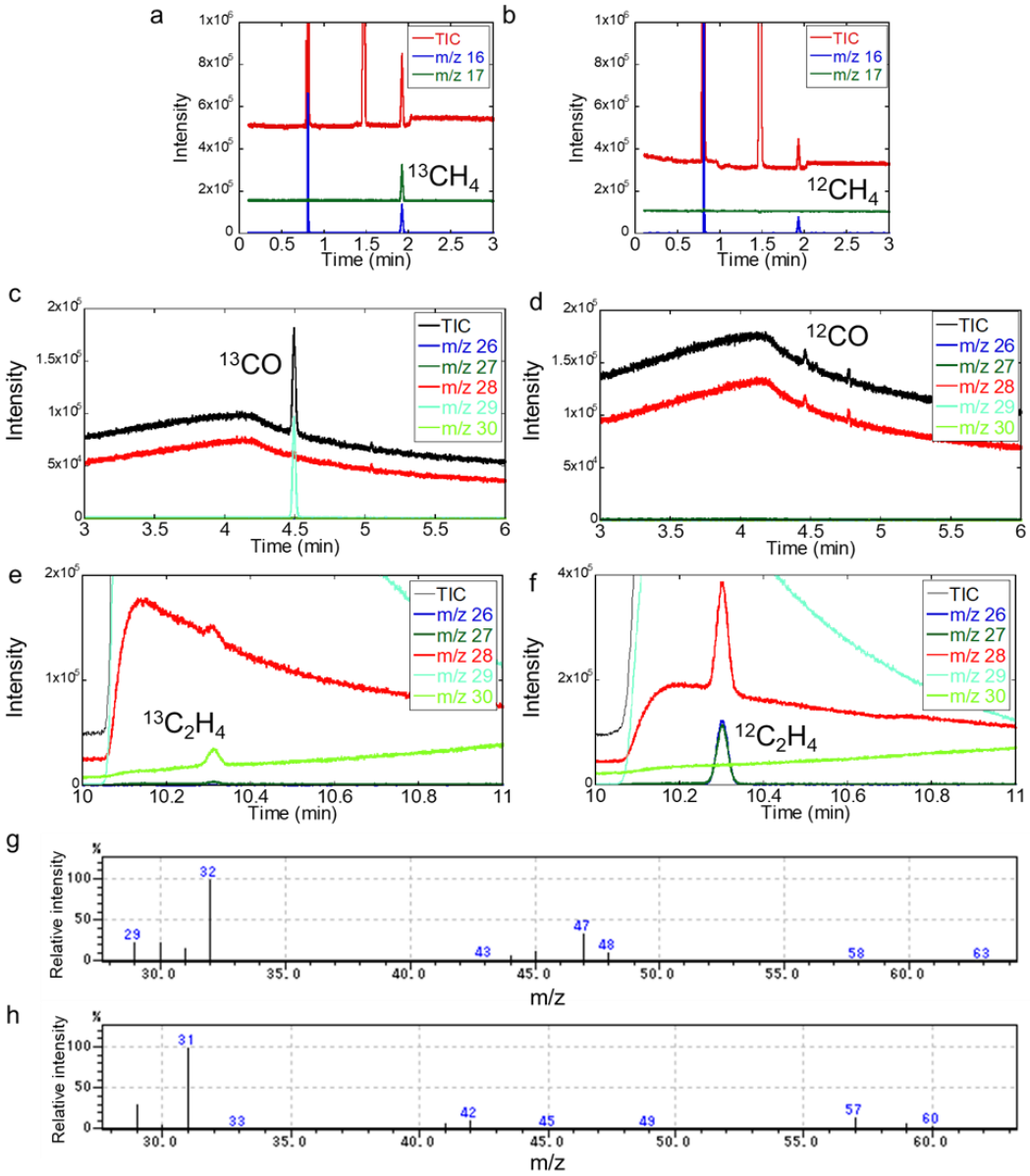

Supplementary Fig. 10. a-f, Gas chromatograms of the gas phase, where MS was used to detect CH_4, CO, and C_2H_4. Gas chromatograms **a**,**c**,**e** for the $^{13}CO_2$ and **b**,**d**,**f** of the $^{12}CO_2$, respectively. **g, h**, GC–MS spectra of the $^{13}CO_2$ and $^{12}CO_2$, respectively.

The *m*/*z* 17, *m*/*z* 29, and *m*/*z* 30 signals, which correspond to $^{13}CH_4$, ^{13}CO, and $^{13}C_2H_4$, respectively, were observed at retention times of 1.9, 4.45, and 10.3 min, respectively. As in the literature[16], in CH_4 and C_2H_4, segments due to H desorption were confirmed. For the peak derived from $^{13}CO_2$, the peak is shifted by the amount replaced by ^{13}C and the peak derived from $^{12}CO_2$ was not confirmed; therefore, the CO_2 reduction product was derived from $^{13}CO_2$.

For propanol, isotope experiments were performed using GC-MS. When non-isotope-labeled CO_2 was used as the reactant, the retention time was the same as that when isotope-labeled CO_2 was used (the mass spectrum showed the signals of $CH_3CH_2CH_2OH$ (*m*/*z* = 60) and a fragment signal (*m*/*z* = 31, 45). When ^{13}C-labeled CO_2 was used, the signals in the mass spectrum shifted to $^{13}CH_3{}^{13}CH_2{}^{13}CH_2OH$ (*m*/*z* = 63) and a fragment signal (*m*/*z* = 32, 47). These results confirmed that the product propanol did not originate from organic impurities or carbonaceous materials, but from the electroreduction reaction of the feed CO_2.

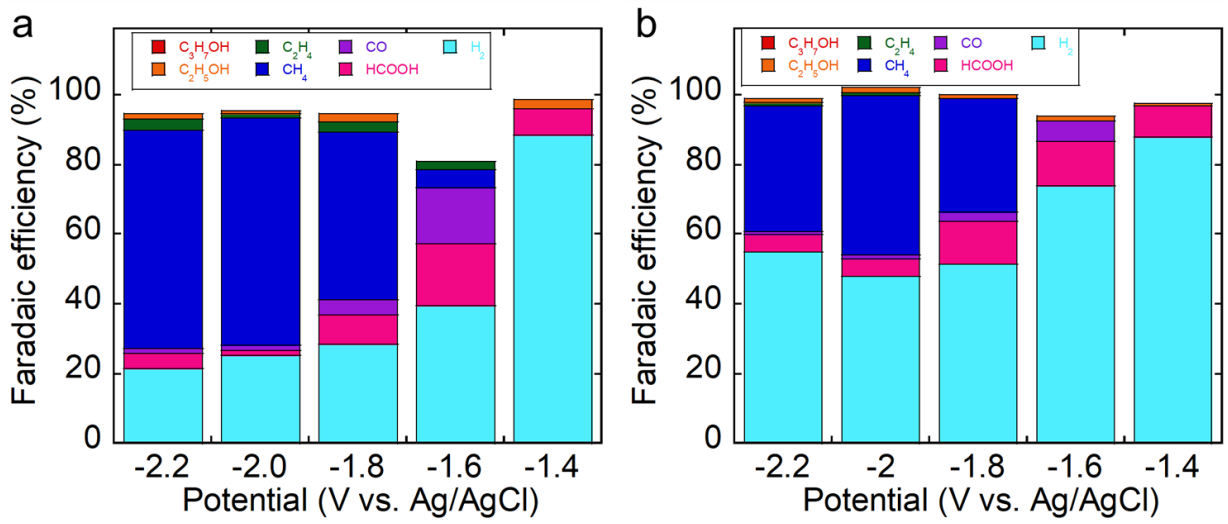

Supplementary Fig. 11. Faradaic efficiency of various reduction products observed after CO_2 reduction for 1 h using **a** CuBr-12B and **b** CuBr-BisM electrodes, respectively, in 0.5 M $KHCO_3$ electrolyte.

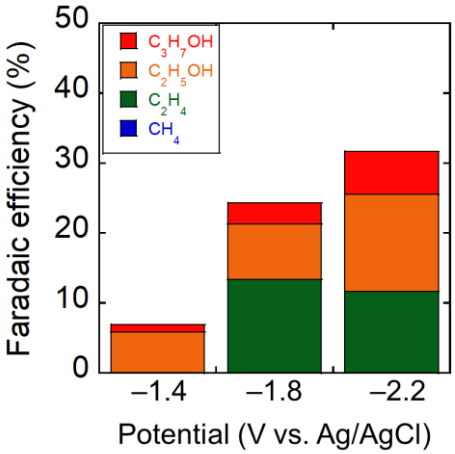

Supplementary Fig. 12. Faradaic efficiency of various reduction products observed after carbon monoxide (CO) reduction for 1 h using the CuBr-4PP electrodes in 0.5 M $KHCO_3$ electrolyte. Other products observed in CORR were CH_3COOH, C_2H_5CHO and $CH_3COOC_2H_5$.

Since CO is less water soluble than CO_2, the formation of H_2 proceeds and the Faraday efficiency of the carbon-containing products is reduced compared to CO_2 reduction. As with CO_2RR, C_2H_4, C_2H_5OH, and C_3H_7OH were produced (Supplementary Fig. 12). The characteristic differences are that no CH_4 formation was observed during CORR, only C_{2+} products were detected. The difference in CH_4 formation between CO_2RR and CORR suggests that the C-C coupling reaction and the C-H bond formation reaction proceed competitively. CH_4 should be produced when C-H coupling proceeds preferentially, but when CO was directly supplied, C-C coupling probably proceeded in advance of C-H coupling. Therefore, even among the many possible branches of C-C and C-H coupling within the CO_2 reduction process, the process observed in the CO reduction is likely to extract the reaction pathway leading to C_3H_7OH.

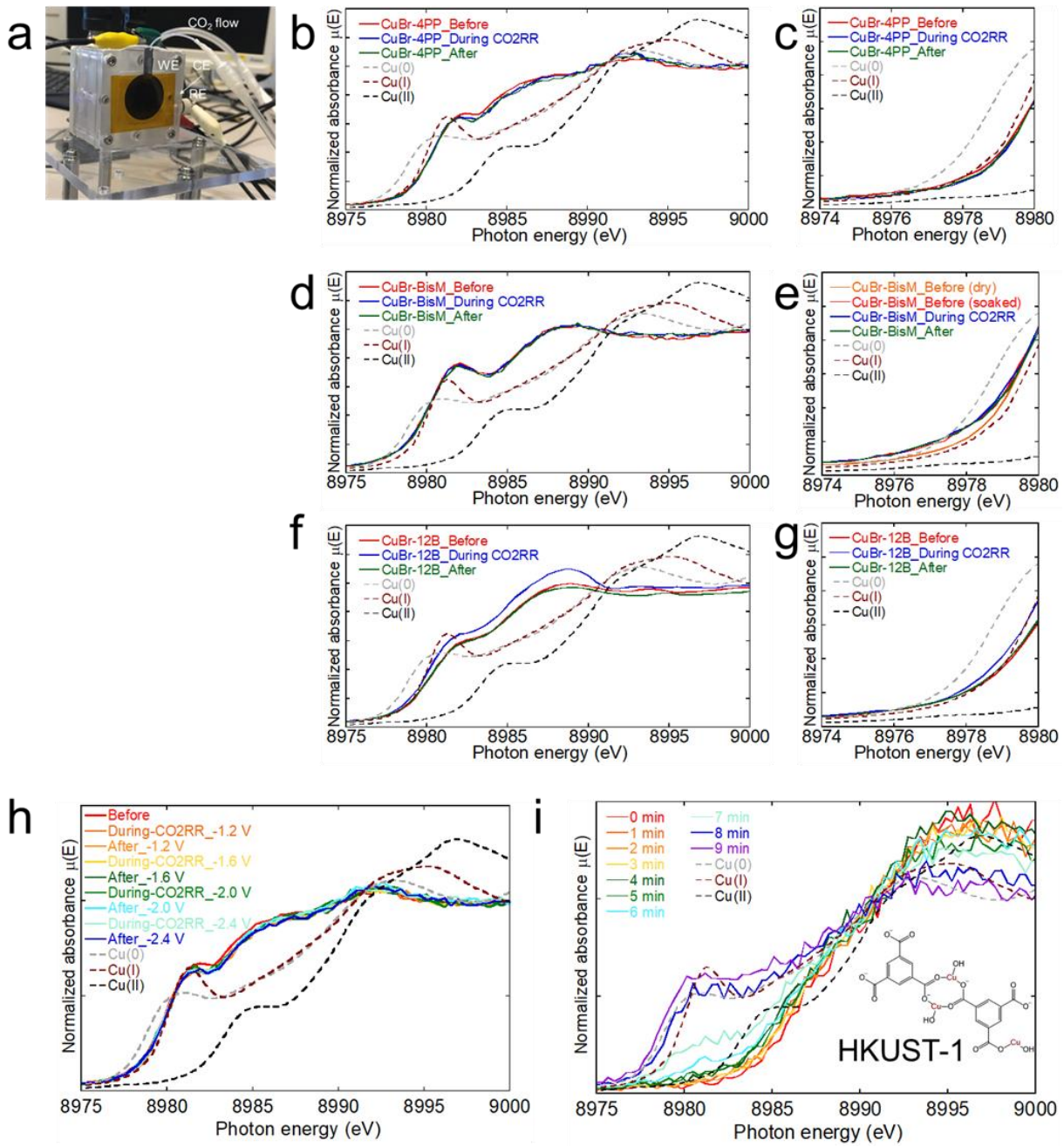

Supplementary Fig. 13. a, *Operando* XAFS experiment setup. **b-g**, *Operando* Cu-K edge XANES spectra for CuBr-4PP, CuBr-BisM and CuBr-12B, respectively, at −2.0 V vs. Ag/AgCl in 0.5 M $KHCO_3$ electrolyte. **c,e,g,** Expanded standing peak positions. **h** *Operando* Cu K-edge XANES spectra for CuBr-4PP electrode at various potentials. **i** *Operando* Cu K-edge XANES spectra for a HKUST-1 electrode at −2.0 V vs. Ag/AgCl in 0.5 M $KHCO_3$ electrolyte.

Operando XANES spectra recorded approximately every 5 min. In the figure, "Before" shows the state soaked in the electrolyte before the reaction, "During CO_2RR" shows the spectrum recorded from 5 to 10 minutes after the reaction begin, and "After" shows the state immediately after the end of voltage application. The spectra for Cu, Cu_2O, and CuO are also shown for reference. Before (dry) in Supplementary Fig. 13e shows the pristine state before CO_2RR.

CuBr-BisM (Supplementary Fig. 13d, e) was attributed to Cu(0) state was maintained during the reaction and after a potential was applied. The pristine CuBr-BisM on electrode before CO_2RR was attributed to Cu(I) (Supplementary Fig. 13e), immediately after contact with the electrolyte, it was shifted to the low energy side and become close to Cu(0) (Supplementary Fig. 13e_soaked).

The CuBr-BisM with active Cu_3Br_2 sites is assumed to have a brittle catalyst because of the insufficient number of Br bridges relative to Cu. Absorption onset in the spectrum of CuBr-12B also changed from the Cu(I) position to lower energy during the reaction; however, it returned to the Cu(I) position soon at the end of electrochemical reaction (Supplementary Fig. 13f, g). This reversible change in oxidation state is similar to those reported for other CH_4-generating molecular catalysts[3].

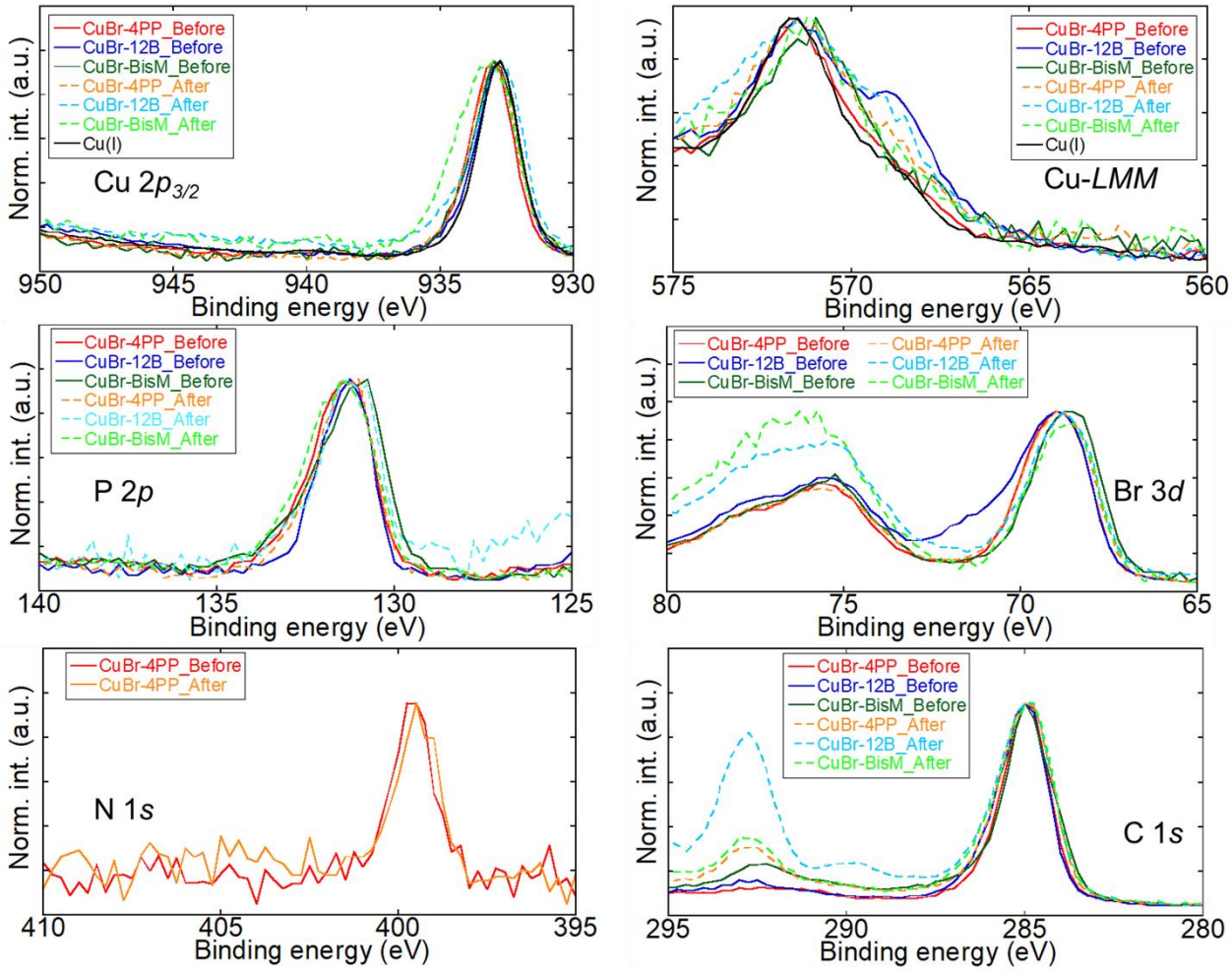

Supplementary Fig. 14. XPS spectra of CuBr-4PP, CuBr-12B, and CuBr-BisM before and after the CO_2 reduction reaction in 0.5 M $KHCO_3$ electrolyte. The spectra were normalized at the most intense peak. The charge-up correction using the C 1*s* 285 eV peak is also shown.

The Cu $2p_{3/2}$ peak and Cu-*LMM* peak in the XPS spectra of CuBr-BisM and CuBr-12B were broadened after the CO_2RR (Supplementary Fig. 14), suggesting decomposition, as observed in the *operando* XAFS experiments.

Supplementary Table 10. Calculated first and second vertical electron affinities in eV

Complex	Without PCM		With PCM	
	First VEA	Second VEA	First VEA	Second VEA
CuBr-4PP	0.26	-3.01	1.79	0.55
CrBr-12B	-0.48	-2.90	0.80	0.42

The calculated first and second vertical electron affinities (VEAs) are shown in Supplementary Table 10. Complexes with a low VEA are difficult for electrons to enter, and, even if electrons do enter, they are unstable because of their high energy. The first VEA and sum of first and second VEA values of CuBr-4PP are higher than that of CuBr-12B. These results suggest that CuBr-4PP exhibits greater electron-accepting ability than CuBr-12B and that its multi-electron reduced state is more stable than that of CuBr-12B.

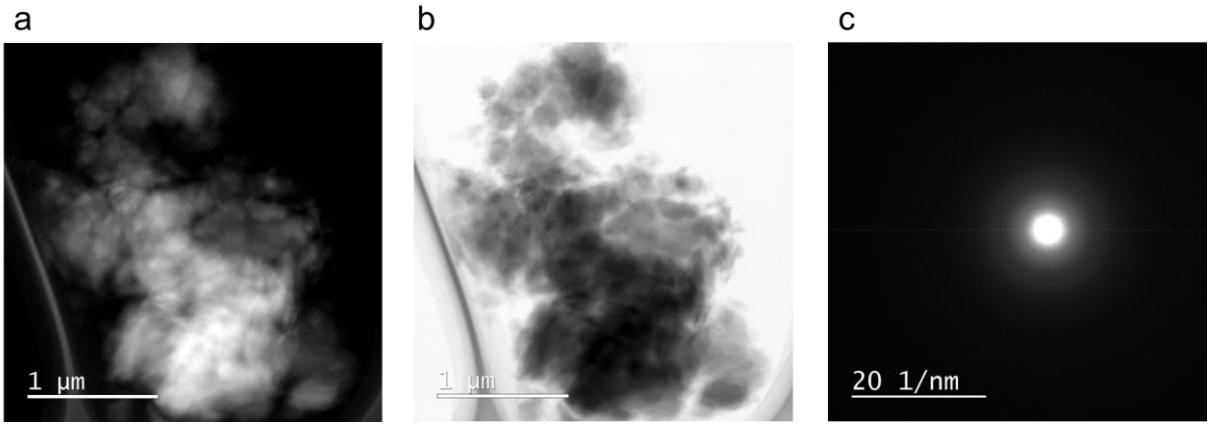

Supplementary Fig. 15. a Dark-field, **b** bright-field TEM images and **c** electron diffraction pattern for CuBr-4PP after the CO_2 reduction reaction.

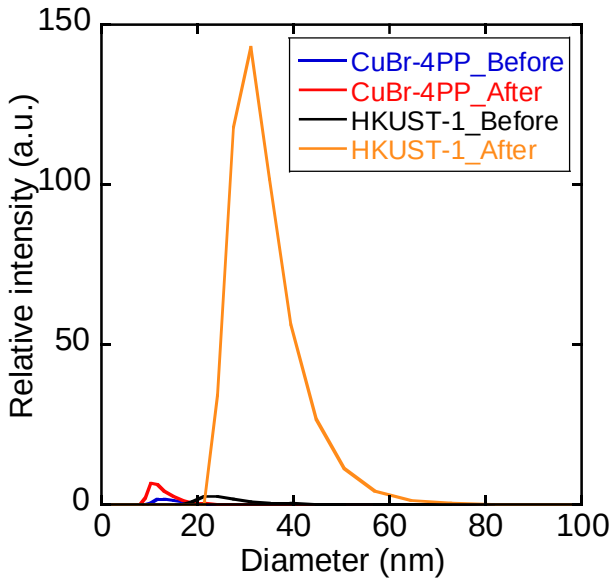

Supplementary Fig. 16. Dynamic light scattering (DLS) experiments showing the particle size distributions of the electrolyte solutions before and after electrolysis. The before-electrolysis solutions are 0.5 M $KHCO_3$ with soaking electrode loaded with molecular catalyst for 1 hour. The after-electrolysis solutions are 0.5 M $KHCO_3$ with soaking the electrode and applying potential of −2.0 V vs. Ag/AgCl for 1 hour. The relative intensities are compared between samples based on scattering intensity (kilo counts per second).

As a reference to form Cu metal, we measured the electrolyte in the electrolysis by HKUST-1. As shown in the black line in Supplementary Fig. 16 without electrolysis, we observed a weak scattering due to the particle size of around 21 nm. With electrolysis of −2.0 V vs. Ag/AgCl (orange line), the size increased to about 31 nm, and the scattering intensity largely increased.

In the electrolyte in which the CuBr-4PP electrode was immersed, no change in particle size was observed, although there was an increase in scattering intensity due to electrolysis (blue line vs. red line). This may be due to the catalysts detached intact due to the gas production by CO_2 electrolysis.

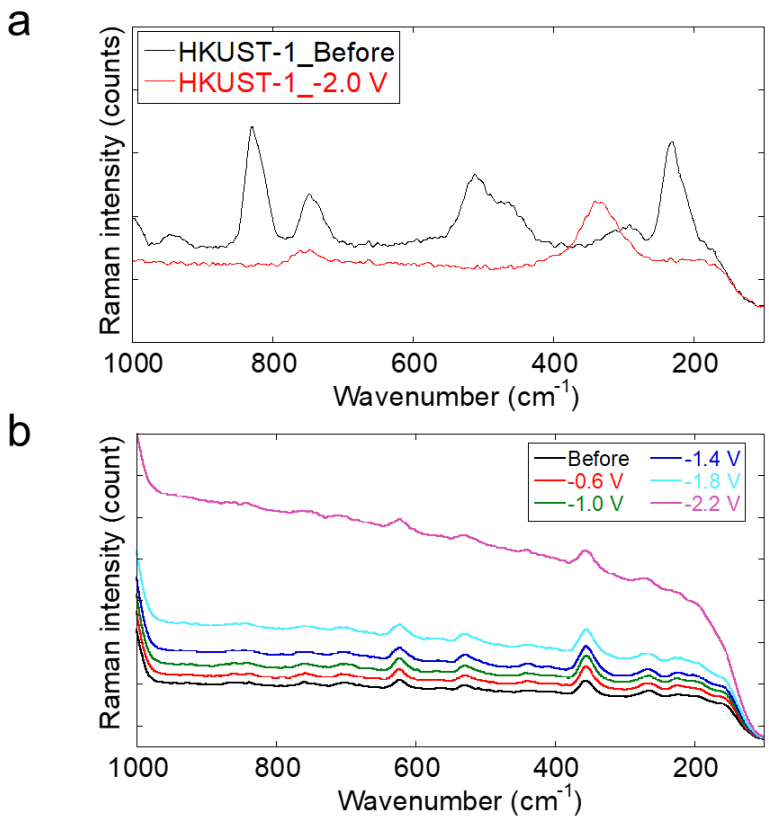

Supplementary Fig. 17. a, *Operando* Raman spectra in the ranges 100–1000 cm^{-1} for HKUST-1 in CO_2. **b,** *Operando* SERS spectra in the ranges 100–1000 cm^{-1} for CuBr-4PP in CO_2.

For HKUST-1 as a reference, for which the formation of Cu clusters was confirmed by *operando* XAFS, *operando* Raman was measured while performing the same electrolysis at −2.0 V vs Ag/AgCl. As shown by the black line in Supplementary Fig. 17a, the electrode before electrolysis exhibited multiple peaks at 230, 460, 510, 830, 940, and 1000 cm^{-1} derived from the 1,3,5-benzenetricarboxylate ligand. However, after electrolysis as shown by the red line in Supplementary Fig. 17a, all these peaks were disappeared. Although Raman-inert Cu metal is not detectable (146, 217, 310, 417, 520, 636, 810 cm^{-1} for Cu_2O and 298, 345, 632 cm^{-1} for CuO[17]), the spectra suggest that ligand would desorb and elute into the solution. In contrast, no peaks attributable to Cu metal were observed in both *operando* SERS (Supplementary Fig. 17b) measurements of CuBr-4PP.

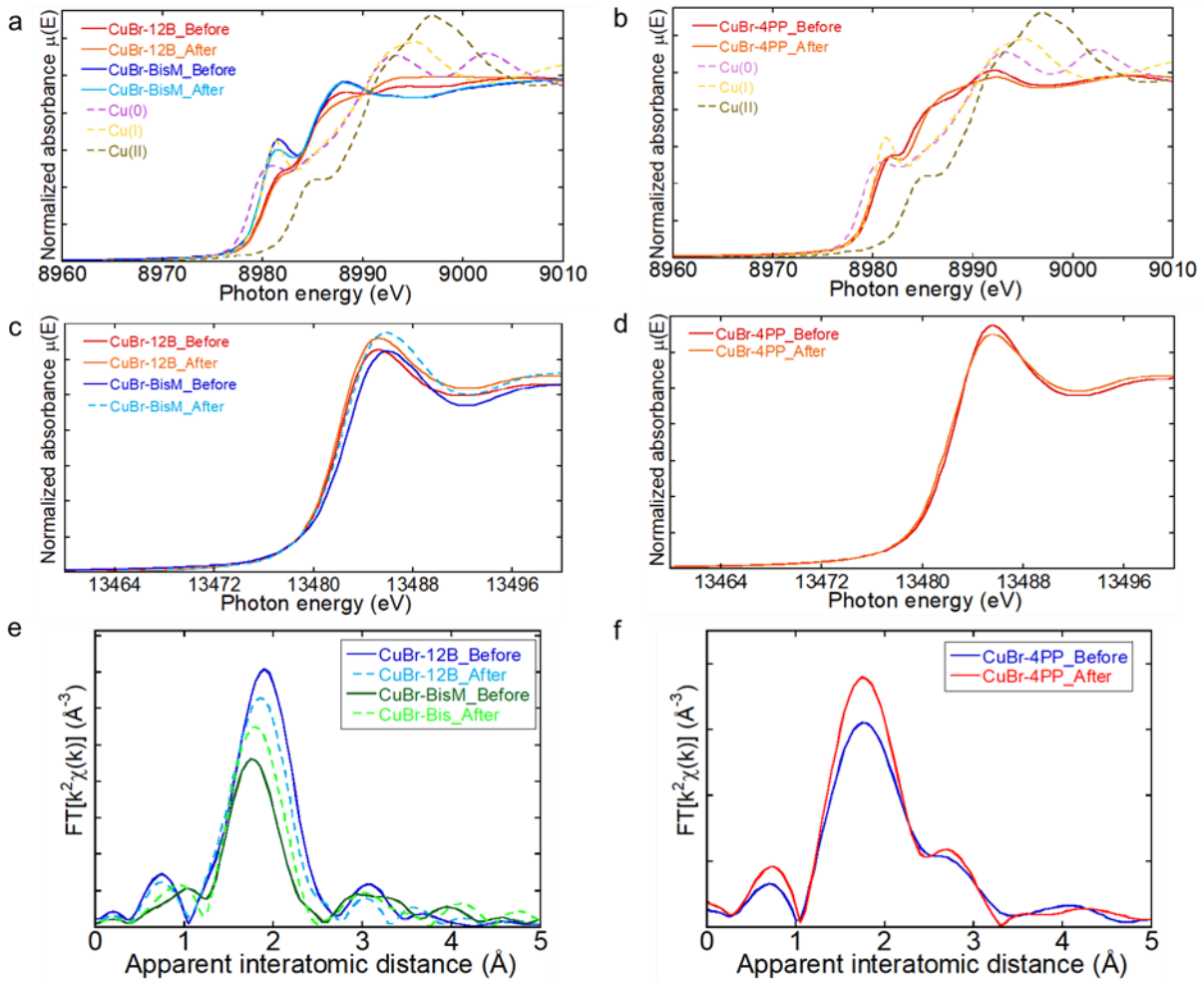

Supplementary Fig. 18. a-b, *Ex situ* Cu K-edge XANES spectra for CuBr-BisM (**a**), CuBr-12B (**a**), and CuBr-4PP (**b**), recorded before and after the CO_2 reduction reaction. The spectra for Cu, Cu_2O, and CuO are also shown for reference. **c,d**, Br K-edge XANES spectra for CuBr-BisM (**c**), CuBr-12B (**c**), and CuBr-4PP (**d**), recorded before and after the CO_2 reduction reaction. **e-f**, EXAFS spectra of the Cu K-edge for CuBr-BisM (**e**), CuBr-12B (**e**), and CuBr-4PP (**f**) electrodes are also shown.

CuBr-BisM, CuBr-12B, and CuBr-4PP have absorption edges that well match that of the Cu_2O reference, which suggests that the Cu atoms in the CuBr-BisM, CuBr-12B, and CuBr-4PP exist mostly in the Cu(I) state (Supplementary Fig. 18a, b). Br K-edge XANES (Supplementary Fig. 18c, d) also showed no significant change in the bridging Br element. The Fourier transform (FT) of the extended X-ray absorption fine structure (EXAFS) spectra (Supplementary Fig. 18e) show no change in CuBr-12B and CuBr-BisM to Cu(0). The EXAFS spectra (Supplementary Fig. 18f) shows that the atomic distance of CuBr-4PP did not change before and after the reaction.

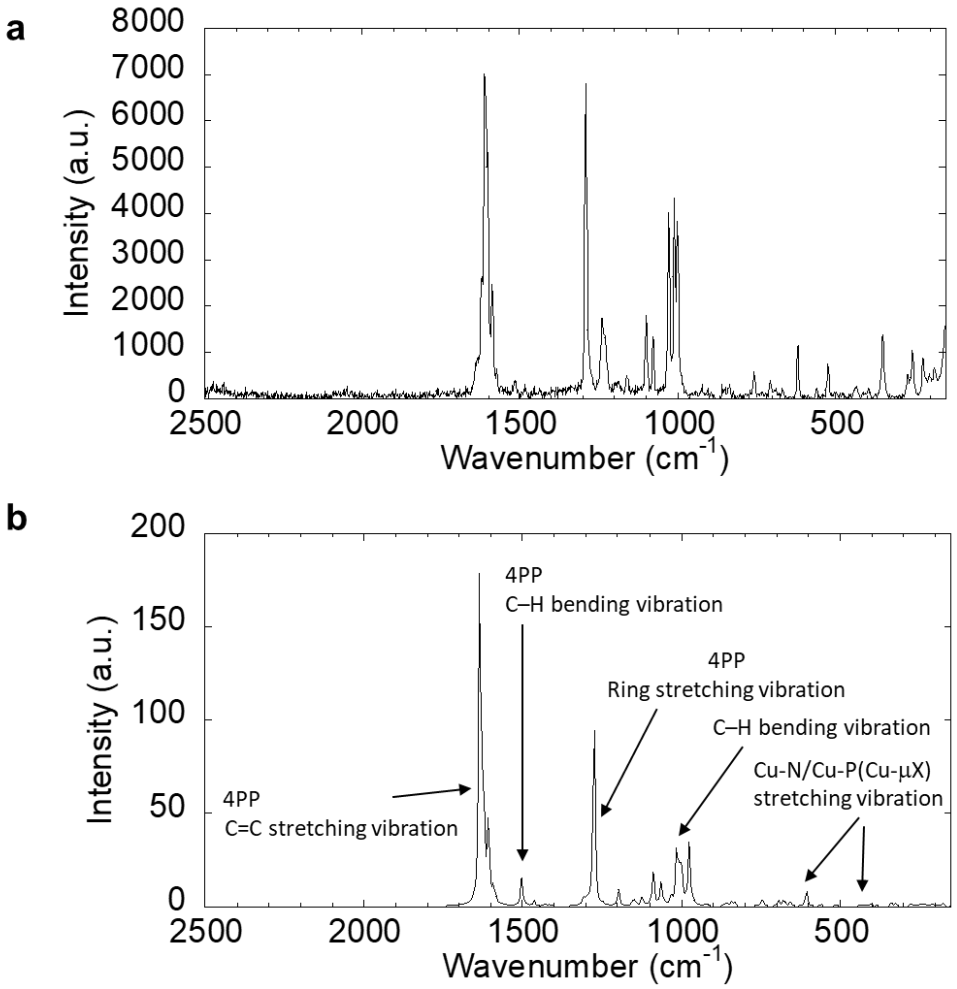

Supplementary Fig. 19. a, Raman spectrum of CuBr-4PP. **b**, The corresponding DFT-calculated Raman frequencies. The values obtained by multiplying the calculated frequencies by a scaling factor of 0.957.

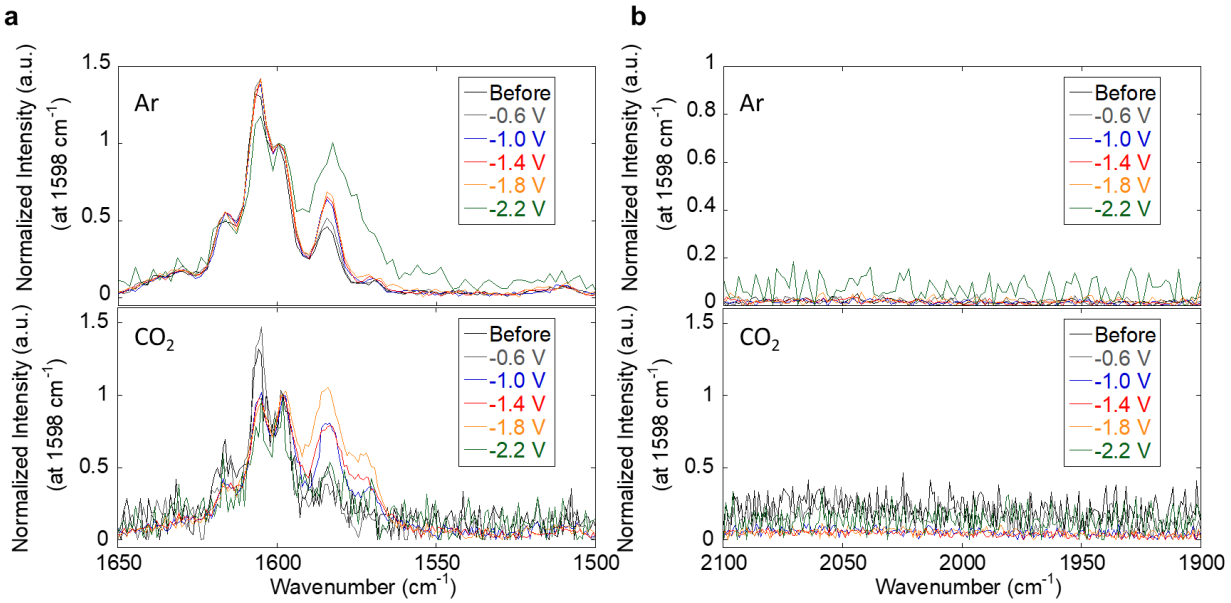

Supplementary Fig. 20. a,b, *Operando* Raman spectra in the ranges 1500–1650 cm^{-1} (**a**) and 1900–2100 cm^{-1} (**b**).

The three peaks at 1585, 1598, and 1605 cm^{-1} are attributed to the C=C stretching vibration of phenyl-pyridine (i.e., C_1–C_4 of the 4PP ligand). For the sample under an Ar atmosphere, the relative vibrational intensities of 1585 and 1598 cm^{-1} were observed at applied potentials at −2.2 V. By contrast, for the under a CO_2 atmosphere, the relative vibrational intensity was enhanced at an applied potential of −1.0 V. The enhancement of the peak intensity observed at the low-energy side presumably reflects the previously reported[18] blue shift due to kinetic suppression. All of the peaks were observed only at the positions in the spectrum of the sample under static conditions (Supplementary Fig. 20b).

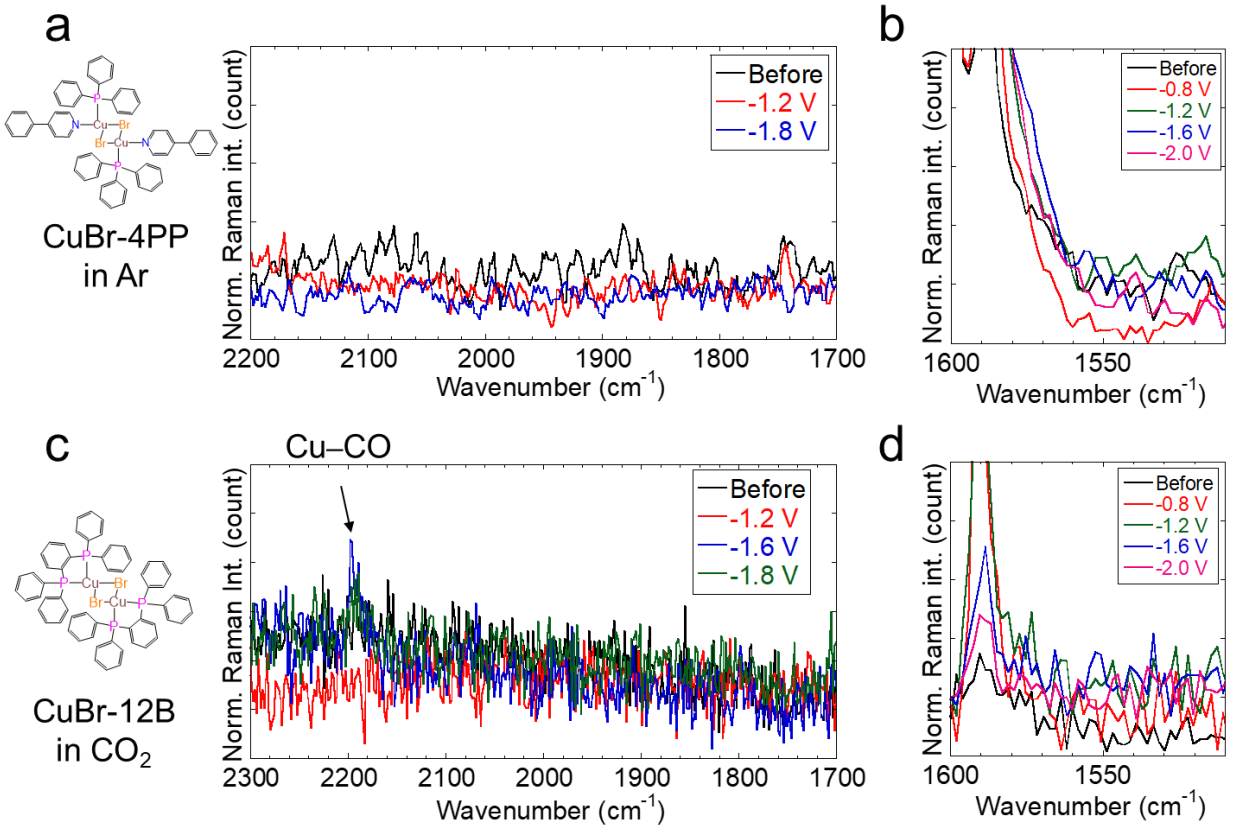

Supplementary Fig. 21. *Operando* SERS spectra for CuBr-4PP under an Ar atmosphere (ranges 1700–2200 cm^{-1} (**a**) and 1510–1600 cm^{-1} (**b**)) and CuBr-12B under a CO_2 atmosphere (ranges 1700–2300 cm^{-1} (**c**) and 1510–1600 cm^{-1} (**d**)).

In contrast to the spectrum of CuBr-4PP under a CO_2 atmosphere (Fig. 3b,c), that of CuBr-12B (Supplementary Fig. 21c,d) shows no peaks at 1750, 2050, and 1500-1560 cm^{-1}, which are attributed to structures bridged by the substrate, such as $[Cu\text{-}CO\text{-}Cu]^{+}$, $[Cu\text{-}CHO\text{-}Cu]^{+}$, $[Cu\text{-}CHOCO\text{-}Cu]^{0}$, $[Cu\text{-}CHOCOH\text{-}Cu]^{0}$, and $[Cu\text{-}CHOCOHCO\text{-}Cu]^{0}$. Combined with the fact that CuBr-12B did not produce C_{2+} products (Supplementary Fig. 11a), these bridging intermediates of CuBr-4PP should be the key structures for C-C coupling. A high wavenumber peak was observed at 2190 cm^{-1} in the spectrum of both CuBr-12B (Supplementary Fig. 21c) and CuBr-4PP (Fig. 3b) when a potential more negative or equal to −1.6 V was applied. This peak is attributed to non-bridged, monodentate Cu-CO, because the high wavenumber suggests that the π back donation from Cu to the antibonding orbital of CO should be small, i.e., very weakly coordination[19]. This monodentate Cu-CO or other Raman-inactive species may result in the formation of methane.

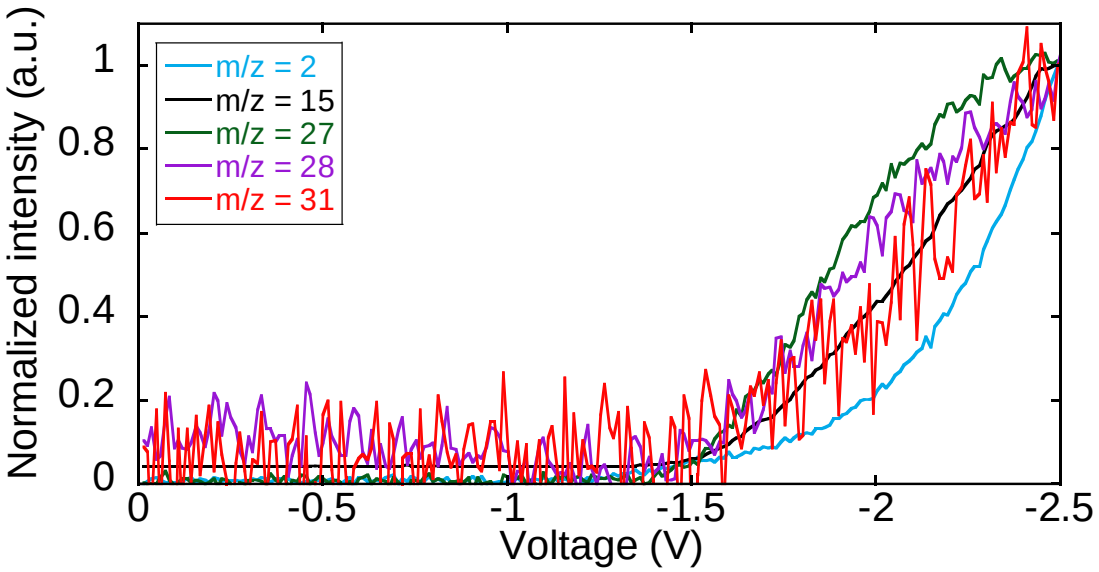

Supplementary Fig. 22. Initial peak potential using differential electrochemical mass spectroscopy results obtained from cyclic voltammograms for CuBr-4PP electrode in 0.5 M $KHCO_3$ electrolyte. The time course of the observed signal at m/z = 2 (H_2), m/z = 15 (CH_4), m/z = 27 (C_2H_4), m/z = 28 (CO, C_2H_4), and m/z = 31 (C_2H_5OH and C_3H_7OH). The signal intensity of m/z = 2, 15, 27, 28 and 31 are normalized at −2.5 V vs. Ag/AgCl.

In the *operando* SERS spectra, peaks attributed to Cu–CO, Cu-C(=O)–(CHO)-Cu, Cu-(CHO)-Cu and Cu-C(=O)–C(OH)–(CHO)-Cu are observed at −1.2 V. According to the DEMS and constant-potential electrolysis results, however, CO_2RR products are produced in the approximate range from −1.4 to −1.5 V.

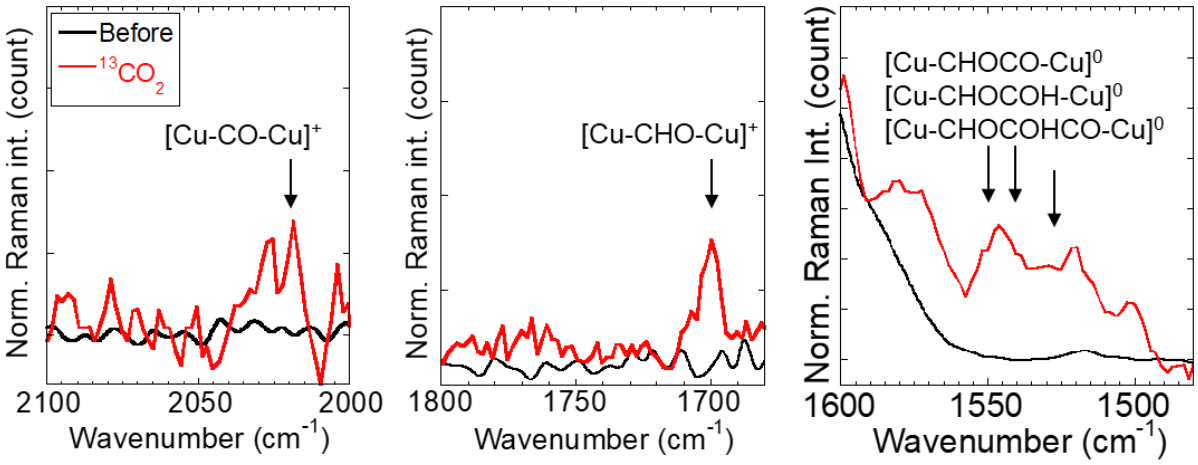

Supplementary Fig. 23. *Operando* SERS spectra for CuBr-4PP under a $^{13}CO_2$. In the $^{13}CO_2$ isotope labeling experiment, the conditions for the potential (The peak around 1470-1600 cm^{-1} is at −2.0 V vs. Ag/AgCl, and the other peaks are at −1.8 V vs. Ag/AgCl applied) at which the SERS peak appears, the cell, and the electrolyte are the same as in the $^{12}CO_2$ experiment.

Fig. 3b-c and Supplementary Fig. 23 compares the spectra observed at $^{12}CO_2$ and $^{13}CO_2$ in the *operando* SERS, where peaks around 1740 and 2050 cm^{-1} are observed under $^{12}CO_2$, whereas peaks in the lower wavenumber region within 50 cm^{-1} appear under $^{13}CO_2$. Under $^{12}CO_2$, multiple peaks were observed in the region of 1520-1570 cm^{-1}, which was difficult to distinguish, but under $^{13}CO_2$, the peaks in this region spread to lower wavenumbers, and therefore peaks above 1500 cm^{-1} were observed. Therefore, this result strongly supports that the peaks at 1520-1560, 1740, and 2050 cm^{-1} observed in the *operando* SERS under $^{12}CO_2$ are derived from intermediates of the CO_2RR.

Supplementary Table 11. Frequency of vibration modes derived from CO stretching in CuBr-4PP and the charge densities of the Cu centers obtained by DFT calculations for each intermediate. The values obtained by multiplying the calculated frequencies by a scaling factor of 0.957.

	Structure	ν^{12}_{CO} **(cm^{-1})**	ν^{13}_{CO} **(cm^{-1})**	Charge Densities of Cu	
1	[Cu-Br-Cu]^0			0.205	0.309
2	[Cu-Br_CO-Cu]$^+$	2126	2077	0.201	0.220
3	[Cu-CO-Cu]$^+$	2047	2001	0.122	0.138
4	[Cu-CHO-Cu]$^+$	1721	1685	0.219	0.294
5	[Cu-CHOCO-Cu]$^+$	1781	1741	0.230	0.266
6	[Cu-CHOCO-Cu]^0	1546	1512	0.204	0.205
7	[Cu-CHOCOH-Cu]^0	1569	1528	0.233	0.271
8	[Cu-CHOCOHCO-Cu]^0	1536	1500	0.369	0.455

The molecular structure was optimized for each model, and the vibrational analysis was carried out at the optimized geometry. A CO_2 molecule was also calculated in the same manner to verify the calculation accuracy and estimate a scaling factor for correction of the calculated vibrational frequencies. The CO_2RR/CORR mechanism on the Cu surfaces has been investigated both experimentally and theoretically, and intermediates appearing during the reaction have been estimated.[20–36] On the basis of the results of these previous studies, we assumed the intermediates of the CO_2RR with CuBr-4PP and calculated their molecular structures and vibrational modes. The calculated and experimental frequencies of the CO antisymmetric stretching were 2267.0 and 2169.8 cm^{-1}, respectively. The calculated frequencies were then multiplied by a scale factor of 0.957. The calculated frequencies were in the range from 1500 to 2100 cm^{-1}, in good agreement with the experimental spectra.

The Mulliken charge densities of the Cu center obtained from DFT calculations for each intermediate in this reaction mechanism yielded charge densities of 0.205 and 0.309 for the initial state of [Cu-Br-Cu]^0. While there were some fluctuations in the charge densities during the reduction reaction, the range between 0.122 to 0.455. This means that Cu did not change significantly from its initial +1 state to 0 or +2 state, which is consistent with the *operando* XAFS results showing that Cu remains in the +1 state.

Supplementary Table 12 Gibbs energy and spin contaminant of the intermediates calculated for each spin multiplicity. Calculated for species with even number of electrons for singlet (S) and triplet (T), and for odd numbers for doublet (D) and quartet (Q).

	Spin state	Energy	$\langle \hat{S}^2 \rangle$ before and after annihilation			
		ΔG(S-T or D-Q) /Hartree	lower spin		higher spin	
			before	after	before	after
$[Cu\text{-}Br\text{-}Cu]^0$	S/T	-0.118223	-	-	2.0240	2.0003
$[Cu\text{-}Br\_CO\text{-}Cu]^0$	S/T	-0.111191	-	-	2.0239	2.0003
$[Cu\text{-}CO\text{-}Cu]^+$	S/T	-0.104536	-	-	2.0549	2.0018
$[Cu\text{-}CHO\text{-}Cu]^+$	D/Q	-0.118615	0.7559	0.7500	3.7892	3.7506
$[Cu\text{-}CHOCO\text{-}Cu]^+$	D/Q	-0.063860	0.7605	0.7501	3.7662	3.7501
$[Cu\text{-}CHOCO\text{-}Cu]^0$	S/T	-0.017905	-	-	2.0130	2.0001
$[Cu\text{-}CHOCOH\text{-}Cu]^0$	D/Q	-0.085491	0.7584	0.7500	3.7989	3.7511
$[Cu\text{-}CHOCOHCO\text{-}Cu]^0$	D/Q	-0.063119	0.7563	0.7500	3.7634	3.7501

Supplementary References

1. Balamurugan, M. *et al.* Electrocatalytic reduction of CO_2 to ethylene by molecular Cu-complex immobilized on graphitized mesoporous carbon. *Small* **16**, 2000955 (2020).
2. Gonglach, S., *et al.* Molecular cobalt corrole complex for the heterogeneous electrocatalytic reduction of carbon dioxide. *Nat. Commun.* **10**, 3864 (2019).
3. Weng, Z. *et al.* Active sites of copper-complex catalytic materials for electrochemical carbon dioxide reduction. *Nat. Commun.* **9**, 415 (2018).
4. Zhu, Q., *et al.* Carbon dioxide electroreduction to C_2 products over copper-cuprous oxide derived from electrosynthesized copper complex. *Nat. Commun.* **10**, 3851 (2019).
5. Bose, P., Mukherjee, C. & Kumar Golder, A. Reduction of CO_2 to value-added products on a Cu(II)-salen complex coated graphite electrocatalyst. *ChemistrySelect* **5**, 9281 (2020).
6. Lu, Y.-F. *et al.* Predesign of catalytically active sites via stable coordination cluster model system for electroreduction of CO_2 to ethylene. *Angew. Chem. Int. Ed.* **60**, 26210 (2021).
7. Weng, Z. *et al.* Electrochemical CO_2 reduction to hydrocarbons on a heterogeneous molecular Cu catalyst in aqueous solution. *J. Am. Chem. Soc.* **138**, 8076–8079 (2016).
8. Liu, Y. *et al.* Steering CO_2 electroreduction toward ethanol production by a surface-bound Ru polypyridyl carbene catalyst on N-doped porous carbon. *Proc. Natl. Acad. Sci. U. S. A.* **116**, 26353 (2019).
9. Rigaku Japan, CrystalClear-SM 1.4.0 SP1 (2008).
10. Rigaku Oxford Diffraction, CrysAlisPro Software System (2018).
11. Dolomanov, O. V., Bourhis, L. J., Gildea, R. J., Howard, J. A. K. & Puschmann, H. OLEX2: A Complete Structure Solution, Refinement and Analysis Program. *J. Appl. Crystallogr.*, **42**, 339−341 (2009). Sheldrick, G. M. SHELXT - integrated space-group and crystal-structure determination, Acta Crystallogr., *Sect. A: Found. Adv.*, **71**, 3−8 (2015). Sheldrick, G.M. Crystal structure refinement with SHELXL. *Acta Cryst.* C71, 3-8 (2015).
12. Ishida, H., Tanaka, K., & Tanaka, T. (1987). Electrochemical CO_2 reduction catalyzed by ruthenium complexes $[Ru(bpy)_2(CO)_2]^{2+}$ and $[Ru(bpy)_2(CO)Cl]^{+}$. Effect of pH on the formation of CO and HCOO. *Organometallics*, **6**, 181-186 (1987).
13. Takeda, H., Koike, K., Inoue, H. & Ishitani, O. Development of an Efficient Photocatalytic System for CO_2 Reduction Using Rhenium(I) Complexes Based on Mechanistic Studies, *J. Am. Chem. Soc.* **130**, 2023-2031 (2008).
14. P.J. Linstrom and W.G. Mallard, Eds., NIST Chemistry WebBook, NIST Standard Reference Database Number 69*, National Institute of Standards and Technology*, Gaithersburg MD, 20899 (retrieved March 11, 2024). Niveditha, C. V., Fatima, M. J., & Sindhu, S. Comprehensive interfacial study of potentio-dynamically synthesized copper oxide thin films for photoelectrochemical applications. *J. Electrochem. Soc.* 163, H426–H433 (2016).
15. Sharma, V., Schlücker, S. & Srivastava, S. K. Origin of the blue-shifted hydrogen bond in the vibrational Raman spectra of pyridine–water complexes: A density functional theory study. *J. Raman Spectrosc.* **52**, 1722–1734 (2021).
16. Katayama, Y. *et al.* An in situ surface-enhanced infrared absorption spectroscopy study of electrochemical CO_2 reduction: selectivity dependence on surface C-bound and O-bound reaction intermediates. *J. Phys. Chem. C* **123**, 5951–5963 (2018).
17. Santatiwongchai, J., Faungnawakij, K. & Hirunsit, P. Comprehensive mechanism of CO_2 electroreduction toward ethylene and ethanol: The solvent effect from explicit water–Cu (100) interface models. *ACS Catal.* **11**, 9688–9701 (2021).
18. Cheng, T., Xiao, H. & Goddard, W. A. Full atomistic reaction mechanism with kinetics for CO reduction on Cu (100) from ab initio molecular dynamics free-energy calculations at 298 K. *Proc. Natl. Acad. Sci. U. S. A.* **114**, 1795–1800 (2017).
19. Nie, X., Esopi, M. R., Janik, M. J. & Asthagiri, A. Selectivity of CO_2 reduction on copper electrodes: The role of the kinetics of elementary steps. *Angew. Chem. Int. Ed.* **52**, 2459–2462 (2013).
20. Nie, X., Luo, W., Janik, M. J. & Asthagiri, A. Reaction mechanisms of CO_2 electrochemical

reduction on Cu(111) determined with density functional theory. *J. Catal.* **312**, 108–122 (2014).
21. Montoya, J. H., Shi, C., Chan, K. & Nørskov, J. K. Theoretical insights into a CO dimerization mechanism in CO_2 electroreduction. *J. Phys. Chem. Lett.* **6**, 2032–2037, (2015).
22. Goodpaster, J. D., Bell, A. T. & Head-Gordon, M. Identification of possible pathways for C–C bond formation during electrochemical reduction of CO_2: New theoretical insights from an improved electrochemical model. *J. Phys. Chem. Lett.* **7**, 1471–1477, (2016).
23. Xiao, H., Cheng, T. & Goddard, W. A. Atomistic mechanisms underlying selectivities in C_1 and C_2 products from electrochemical reduction of CO on Cu(111). *J. Am. Chem. Soc.* **139**, 130–136 (2017).
24. Zheng, Y. *et al.* Understanding the roadmap for electrochemical reduction of CO_2 to multi-carbon oxygenates and hydrocarbons on copper-based catalysts. *J. Am. Chem. Soc.* **141**, 7646–7659 (2019).
25. Wang, G. *et al.* Electrocatalysis for CO_2 conversion: from fundamentals to value-added products. *Chem. Soc. Rev.* **50**, 4993–5061 (2021).
26. Wang, Y., Liu, J. & Zheng, G. Designing copper-based catalysts for efficient carbon dioxide electroreduction. *Adv. Mater.* **33**, 2005798 (2021).
27. Ye, W., Guo, X. & Ma, T. A review on electrochemical synthesized copper-based catalysts for electrochemical reduction of CO_2 to C_{2+} products. *Chem. Eng. J.* **414**, 128825 (2021).
28. Herzberg, G., *Molecular spectra and molecular structure. Vol.3: Electronic spectra and electronic structure of polyatomic molecules*. 1966: pp 598.
29. Pablo-García, S. *et al.* N. Mechanistic routes toward C_3 products in copper-catalysed CO_2 electroreduction. *Catal. Sci. Technol.*, **12**, 409-417 (2022).
30. Peng, H. *et al.* The role of atomic carbon in directing electrochemical CO_2 reduction to multicarbon products. *Energy Environ. Sci.* **14**, 473- 482 (2021).
31. Garza, A. J., Bell, A. T., & Head-Gordon, M. Mechanism of CO_2 reduction at copper surfaces: pathways to C_2 products. *ACS Catal.* **8**, 1490-1499 (2018).
32. Birdja, Y.Y., Pérez-Gallent, E., Figueiredo, M.C. *et. al.* Advances and challenges in understanding the electrocatalytic conversion of carbon dioxide to fuels. *Nat Energy* **4**, 732–745 (2019).
33. Ren, H. *et al.* Operando proton-transfer-reaction time-of-flight mass spectrometry of carbon dioxide reduction electrocatalysis. *Nat Catal* **5**, 1169–1179 (2022).